RESEARCH ARTICLE | SEPTEMBER 09 2025

3D bioprinted human iPSC-derived neural progenitor cells as a novel platform for studying neurogenic niche

Lucas Simões Machado ; Paula Scanavez Ferreira ; Marina Rodrigues Pires ; Larissa Valdemarin Bim ; Natália Heloísa de Oliveira ; Geisa Rodrigues Salles ; Natalia Dall'Agnol Ferreira ; Elisa Marozzi Cruz ; Marimelia Aparecida Porcionatto

APL Bioeng. 9, 036116 (2025)
https://doi.org/10.1063/5.0276704

3D bioprinted human iPSC-derived neural progenitor cells as a novel platform for studying neurogenic niche

Cite as: APL Bioeng. **9**, 036116 (2025); doi: 10.1063/5.0276704
Submitted: 19 April 2025 · Accepted: 10 August 2025 ·
Published Online: 9 September 2025

View Online Export Citation CrossMark

Lucas Simões Machado,[1,2] Paula Scanavez Ferreira,[1,2] Marina Rodrigues Pires,[1,2] Larissa Valdemarin Bim,[1,2] Natália Heloísa de Oliveira,[1,2] Geisa Rodrigues Salles,[1,2,a)] Natalia Dall'Agnol Ferreira,[1,2] Elisa Marozzi Cruz,[1,2,b)] and Marimelia Aparecida Porcionatto[1,2,c)]

AFFILIATIONS

[1]Department of Biochemistry, Escola Paulista de Medicina, Universidade Federal de São Paulo (Unifesp), São Paulo 04039-032, Brazil
[2]National Institute of Science, Technology, and Innovation in Modelling Human Complex Diseases with 3D Platforms (INCT Model3D), Universidade Federal de São Paulo (Unifesp), São Paulo 04039-032, Brazil

[a)]**Present address:** Research & Development Institute, Universidade do Vale do Paraíba, São José dos Campos, São Paulo, Brazil.
[b)]**Present address:** Department of Physiology, Anatomy and Genetics, University of Oxford, Oxford OX1 3PT, United Kingdom.
[c)]**Author to whom correspondence should be addressed:** marimelia.porcionatto@unifesp.br

ABSTRACT

Animal models, especially rodents, used to study neurodevelopment have significantly advanced our comprehension of cellular and molecular mechanisms. Nevertheless, differences in species-specific structures, gestation periods, and interneuronal connections limit animal models' ability to represent human neurodevelopment accurately. The unique characteristics of primate neural progenitor cells (NPCs) enable cortex expansion with gyrus formation, which does not occur in lissencephalic animals, like rodents. Therefore, there is a need for novel *in vitro* models using human cells that recapitulate the complexity of human brain development. Along with organoids, 3D bioprinting offers a platform for creating more complex *in vitro* models. We developed, extensively characterized, and successfully used a Geltrex^{TM}/GelMA hydrogel blend to bioprint human induced pluripotent stem cells-derived NPCs (hNPCs). We show that 3D bioprinted hNPCs can self-organize, revealing key features of a neurogenic niche, including proliferation, differentiation, and migration, remaining viable for over 110 days. Within the first 20 days, bioprinted constructs showed the formation of positive cell clusters for the neurogenic niche cell markers FABP7, NESTIN, and GFAP. Clusters were interconnected by process bundles supporting cell migration. The cells proliferated within the clusters, and over time, NPCs originated TUBB3^{+} neurons with long axonal tracts, prominent around the clusters. We propose this as a 4D model to study neurogenic niches' key cellular and molecular features in a 3D bioprinted scaffold, adding time as the fourth dimension. Neuronal maturation in this dynamic model recapitulates key neurogenic niche properties, making it suitable for neurodevelopmental disease modeling and drug screening.

BACKGROUND AND AIM

Much information about human neurogenesis, the process of generating neurons from neural progenitor cells (NPCs), has been gathered from animal models, postmortem or surgically removed human brain tissue, and cell cultures. While animal models provide valuable insights into the cellular and molecular mechanisms that drive neurogenesis, they often fail to fully recapitulate human-specific neurodevelopment, disease pathology, and gene regulation, raising concerns about their translational relevance (Zhang *et al.*, 2023; Zhao and Bhattacharyya, 2018). Additionally, the increasing emphasis on reducing animal use in research presents a challenge in developing alternative models that more accurately mimic the complexity of human neural tissue.

New *in vitro* models and platforms are currently being employed to mimic and study neurogenic niches, including tridimensional (3D) structures such as cortical organoids, neurospheres, and 3D bioprinted

hydrogels, as well as traditional bidimensional (2D) cell cultures (Ioannidis *et al.*, 2021; Lee and Sun, 2022). While the cellular components are critical, acellular elements also play a fundamental role in regulating neurogenic environments. When using bio-based biomaterials, such as hydrogels, to model the 3D architecture of the native brain tissue, material characteristics, such as stiffness and topography, play a key role in supporting cell survival and growth (Gradisnik *et al.*, 2021). The combination of hydrogels and soluble factors provides extracellular cues by activating mechanoreceptors and adhesion receptors, actively modulating cell behavior (Bao *et al.*, 2018).

Cortical organoids, 3D self-organizing cellular structures generated from induced pluripotent stem cells (iPSCs), replicate early brain development and have emerged as one of the most relevant tools for understanding that stage of development (Bektas *et al.*, 2025; Tarricone *et al.*, 2022). Although organoids closely mimic the structure and function of neural tissue, the model's challenges include limited maturation despite prolonged cultivation and absence of vascularization, resulting in insufficient nutrient delivery and waste removal, reducing cell survival (de la Vega *et al.*, 2019). Additionally, organoids may present variable cellular organization, lower cell diversity than the brain, and high variability between batches (Andrews and Kriegstein, 2022; Bose *et al.*, 2021; de Jongh *et al.*, 2022; Hofer and Lutolf, 2021; and Kim *et al.*, 2020).

Conversely, 3D bioprinting provides a more controlled approach to generating neural-like structures that can better reproduce neurogenic niches and other neural structures. Bioinks, a combination of hydrogel and cells, can be accurately deposited to form tissue-like geometries and optimal 3D microenvironments. At the same time, the hydrogel composition can be tailored to provide biochemical, biophysical, and mechanical cues essential for regulating stem cell fate and directing cells toward specific phenotypes (Bektas *et al.*, 2025; de Groot *et al.*, 2020; and de la Vega *et al.*, 2019). By manipulating the mechanical and structural characteristics of the hydrogel, bioinks can exhibit proper porosity and degradability, which enhances the diffusion of gases, ions, and nutrients within the 3D construct, supporting cell viability and simulating the exchange of signals and nutrients (Orr *et al.*, 2025; Salaris and Rosa, 2019).

The main advantages of 3D bioprinting over bulk hydrogels include greater reproducibility, spatial control, and the potential to replicate specific brain structures. Although current 3D bioprinting technologies still face challenges in precisely placing cells at defined locations, ongoing advances are expected to improve resolution and accuracy. A promising application of 3D bioprinting is the reconstruction of lost neural tissue guided by neuroimaging, with the potential to create personalized implants that fit into lesions in the brain or spinal cord. Moreover, 3D bioprinting enables the precise arrangement of multiple cell types—for example, printing neurons and astrocytes in distinct locations—and allows for the incorporation of acellular hydrogel layers to establish gradients of soluble factors or varied extracellular matrix (ECM) components.

Beyond structural advantages, 3D bioprinting human-induced pluripotent stem cells (hiPSCs) provides translationally relevant models of human neural tissue. These systems can offer a powerful platform for studying neurodevelopment and disease progression and can be used for potential regenerative therapies and drug screening (Salaris and Rosa, 2019; Orr *et al.*, 2025; and Soman and Vijayavenkataraman, 2020). Considering these aspects, we aimed to create a 3D bioprinted model of the human neurogenic niche microenvironment employing a hydrogel composition that provides biochemical and mechanical stimuli necessary for cellular growth and differentiation. Thus, in this study, we successfully bioprinted human NPCs (hNPCs) derived from hiPSCs using a hydrogel composed of Geltrex™ and gelatin methacrylate (8% GelMA). We investigated the structural and mechanical properties of the construct, which enabled the self-organization and survival of hNPCs for more than 100 days, uncovering critical characteristics of a neurogenic niche, including cell proliferation, differentiation, and motility.

RESULTS

Structural and mechanical characterization of the hydrogel for 3D bioprinting hNPCs

Assessing the structural and mechanical properties of the hydrogel is essential when creating 3D bioprinted models, particularly when attempting to mimic a specific microenvironment such as the neurogenic niche. The composition of the hydrogel allows the replication of extracellular matrix (ECM) characteristics, such as mechanical cues that govern cellular fate and behavior via cell–ECM mechanotransduction (Kothapalli *et al.*, 2020). As previously described by our group (Cruz *et al.*, 2023), adding Geltrex™ into GelMA-based hydrogel compositions is vital for ensuring a bioink that promotes cellular viability and supports neuronal differentiation of 3D bioprinted hNPCs.

The Geltrex™/GelMA blend (8%GelMA; 1:1, v/v) (Table I lists the reagents used in this study) [Fig. 1(a)] yielded a hydrogel that fulfilled several key requirements for practical application in 3D extrusion-based bioprinting for neural tissue modeling. The hydrogel characteristics include printability, *in situ* gelation, viscoelastic properties, consistent degradability, diffusion of nutrients, and proper mechanical strength and integrity (Figs. 1 and 2). Additionally, the hydrogel presented stiffness that is compatible with maintaining the 3D structure for a defined period while supporting cell viability, migration, proliferation, neuronal differentiation, and neural network formation.

The topography, porosity, and microstructure of the 3D construct, along with cellular morphology and attachment, were assessed using scanning electron microscopy (SEM) analysis of hNPCs bioprinted constructs cultivated for 36 days in neural maturation medium (NMM; Table II) [Figs. 1(d)–1(g)]. The acellular and cell-containing constructs presented a smooth and uniform surface [Figs. 1(d)–1(g)]. After 36 days in culture, cellular protrusions, clusters, and agglomerates emerged throughout the construct, creating a dense and extensive network inside the hydrogel [Figs. 1(d)–1(f)]. Furthermore, the surface morphology of the samples evolved from an initially smooth texture to a more complex and wavy structure.

The hydrogel degradation was followed for 28 days using acellular constructs submerged in phosphate-buffered saline (PBS) (pH 7.4, 10 mM) at 37 °C. On the day of printing (Day 0, D0), the samples exhibited a circular and well-defined 3D structure [Fig. 1(b)]. At D28, the constructs suffered significant weight and 3D integrity loss and became challenging to manipulate [Fig. 1(c)]. In the absence of cells, the rate of degradation reached 50% at D2 [Fig. 1(h)] and constructs lost weight over time, reaching nearly 100% loss at D28. From D0 to D28, the acellular constructs exhibited an increasing swelling rate [Fig. 1(i)], although the values were negative up to D2 due to a substantial initial weight loss (∼50% degradation rate). Despite further

TABLE I. Reagents.

Category	Reagent	Catalogue #	Company	Country
Bioprinting	Geltrex™	A1413302	Gibco	USA
	Gelatin from porcine skin	G2500	Sigma-Aldrich	USA
	Methacrylic anhydride	276685	Sigma-Aldrich	USA
	Irgacure	2959	Sigma-Aldrich	USA
Cell culture	Penicillin/streptomycin	15140122	Gibco	USA
	DMEM/F12	12500-062	Gibco	USA
	Essential E8 medium	A15169-01	Gibco	USA
	Neurobasal medium	21103-049	Gibco	USA
	B27 without vitamin A	12587-010	Gibco	USA
	N2 supplement	17502-048	Gibco	USA
	Glutamax	3505-061	Gibco	USA
	SMAD inhibitor LDN193189	SML0559	Sigma-Aldrich	USA
	SMAD inhibitor SB431542	S4317	Sigma-Aldrich	USA
	StemPro Accutase	A11105-01	Gibco	USA
	EGF	E9644-2MG	Sigma-Aldrich	USA
	bFGF	PHG0026	Gibco	USA
	Ascorbic acid	A4403	Sigma-Aldrich	USA
	db-cAMP	D0627	Sigma-Aldrich	USA
	BDNF	B3775	Sigma-Aldrich	USA
	GDNF	G1777	Sigma-Aldrich	USA
Viability and proliferation assays	LIVE/DEAD™ Cell Imaging Kit	R37601	Sigma-Aldrich	USA
	Resazurin	R7017	Sigma-Aldrich	USA
RT-qPCR	TRIzol™	15596026	Thermo Fisher	USA
	SuperScript™ III First-Strand Synthesis SuperMix	18080400	Thermo Fisher	USA
	Fast SYBR™ Green Master Mix	4385612	Thermo Fisher	USA
Immunofluorescence	Goat serum	S26–100 ml	Merck Millipore	USA
	Rabbit anti-FABP7	PA5-24949	Thermo Fisher	USA
	Rabbit anti-NESTIN	MA5-32272	Thermo Fisher	USA
	Chicken anti-GFAP	ab5541	Merck Millipore	USA
	Mouse anti-TUBB3	MA1-118	Thermo Fisher	USA
	Mouse anti-Ki67	14-5698-82	Thermo Fisher	USA
	AlexaFluor 488-conjugated chicken anti-rabbit	A21441	Invitrogen	USA
	AlexaFluor 594-conjugated donkey anti-mouse	A21203	Invitrogen	USA
	AlexaFluor 647-conjugated goat anti-chicken	A21449	Invitrogen	USA
	DAPI	62248	Sigma-Aldrich	USA

swelling, the ultimate wet weight remained lower than the dry weight, yielding a negative value. The wet weight increased as time progressed, indicating that the samples swelled in response to PBS absorption. This suggests that while the hydrogel degrades over time, it simultaneously absorbs water, potentially enhancing the diffusion of nutrients and gases within the 3D construct.

To assess the hydrogel hydrophilicity or hydrophobicity, we evaluated its wettability properties by measuring the contact angle between the surfaces of the construct and a liquid droplet (Naghieh and Chen, 2021; Sun *et al.*, 2018). A wettable hydrogel is hydrophilic, which may support cellular viability, proliferation, and migration due to the material's adhesion properties (Naghieh and Chen, 2021; Tuft *et al.*, 2014). The acellular constructs exhibited an initial contact angle of around 20°, which diminished to around 18° after 10 min [Figs. 1(k)–1(o)]. Contact angles ranging from 0° to 90° indicate a wettable, hydrophilic surface, whereas angles between 90° and 180° denote a non-wettable, hydrophobic surface (Rodriguez-Rego *et al.*, 2023).

A contact angle <30° indicates a bioink with low surface tension (Naghieh and Chen, 2021). Low surface tension can cause deformation during the layer-by-layer printing process, mixing or fusing the extruded filaments. Hence, high wettability may not be ideal for 3D bioprinting if high shape fidelity is required (Chen *et al.*, 2023; Naghieh and Chen, 2021). Nonetheless, additional mechanical characteristics can also enhance the extrudability and printability, including the flow behavior of the bioink. The high wettability of the Geltrex™/GelMA hydrogel, based on the contact angle of 18–20 °C, may improve cell adhesion

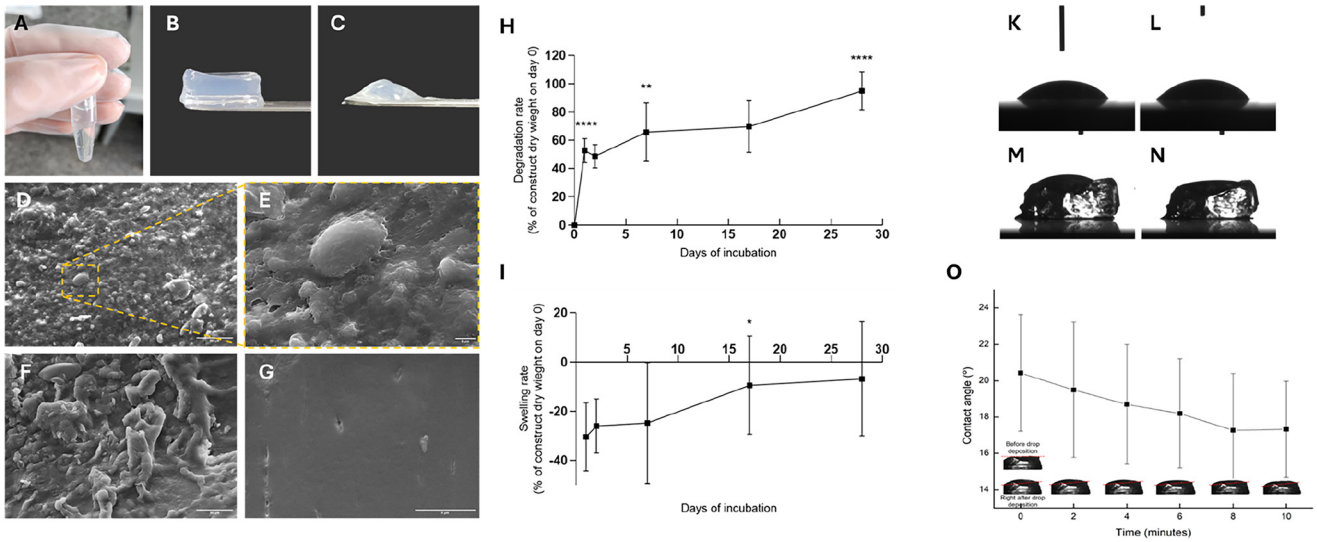

FIG. 1. Physical properties of the hydrogel. (a) Geltrex™/GelMA hydrogel at room temperature before the printing process. (b) Acellular construct immediately after chemical gelation on Day 0 (D0) of the degradation test. (c) Acellular construct on Day 28 (D28) of the degradation test. (d)–(f) Scanning electron microscopy (SEM) analysis of hiPSC-derived NPCs (hNPCs) bioprinted constructs at D36 cultured in neural maturation medium (NMM). (d) Scale bar = 50 μm, (e) scale bar = 5 μm, (f) scale bar = 50 μm. (g) SEM analysis of the acellular construct, scale bar = 5 μm. (h) Degradation rate of acellular constructs in PBS at 37 °C, up to 28 days (n = 9 per time point) ($^{*}p < 0.5$; $^{**}p < 0.01$; $^{****}p < 0.0001$, groups compared to the group immediately before by Bonferroni's post hoc test). (i) Swelling rate of acellular constructs in PBS at 37 °C, up to 28 days (n = 9 per time point) ($^{*}p < 0.5$, groups compared to the group immediately before by Bonferroni's post hoc test). (k) Contact angle analysis before adding a water droplet to the acellular construct surface, (l) where the droplet was immediately absorbed. (m) Water droplet on acellular construct in the first min and (n) after 40 min. (o) Contact angle and wettability periodic scheme of acellular constructs (n = 3 per group).

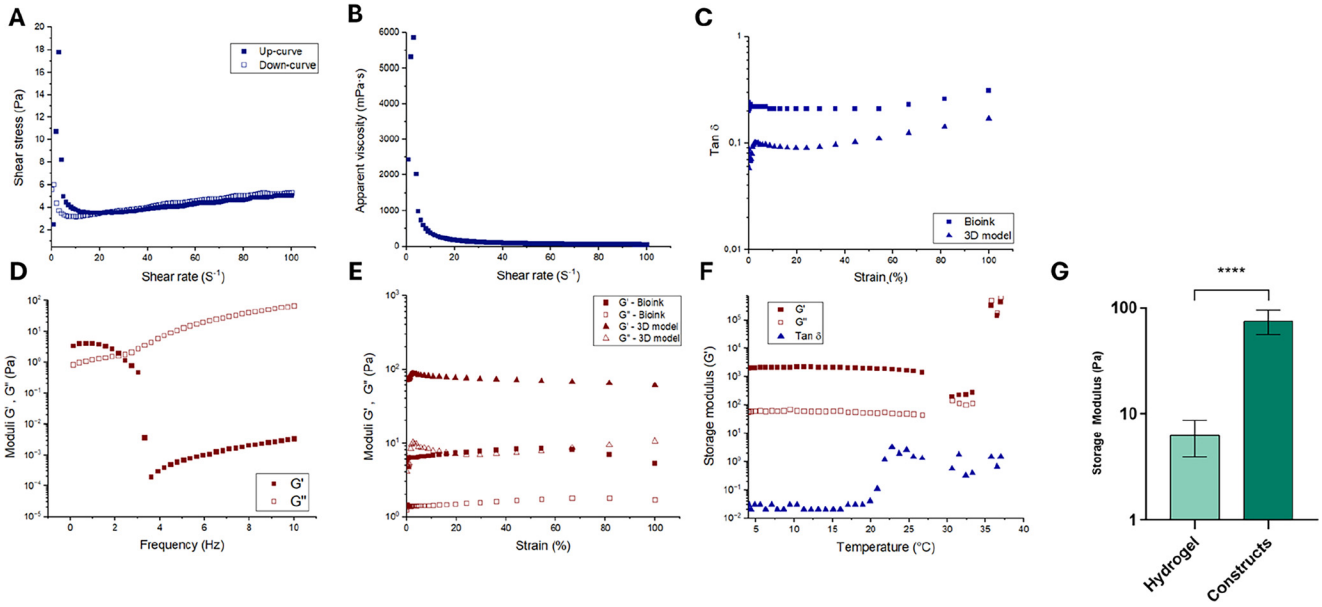

FIG. 2. Rheological properties of the Geltrex™/GelMA hydrogel. (a) Flow behavior displaying minimal thixotropy. Filled symbols indicate an upward curve; empty symbols indicate a downward curve. (b) Viscosity as a function of increasing shear rate reveals the shear-thinning behavior of the hydrogel. (c) Loss factor (tan δ) as a function of oscillatory strain at 25 °C and constant frequency of 1 Hz for both the hydrogel and the acellular construct. (d) and (e) Storage modulus (G′; filled symbols) and loss modulus (G″; empty symbols) obtained from an amplitude sweep test (d) and a frequency sweep test (e) demonstrated the hydrogel's viscoelastic behavior. (f) Storage modulus (G′; square filled symbols), loss modulus (G″; square empty symbols), and tan δ (triangle filled symbols) vs oscillatory temperature sweep under a constant strain of 1% and frequency of 1 Hz. (g) The storage modulus of both hydrogel and the acellular construct at a frequency = 1 Hz and strain = 1%. All rheological measurements, apart from the oscillatory temperature sweep, were conducted at 25 °C. Data are plotted as the mean values from three replicates.

TABLE II. Media composition.

	Medium	Supplement	Growth/neurotrophic factors	Other
Neural induction medium (NIM)	Neurobasal:DMEM/F12 (1:1)	B27 w/o vitamin A N2 1 mM Glutamax		SMAD inhibitors (0.1 μM LDN193189 and 10 μM SB431542)
Neural expansion medium (NEM)	Neurobasal:DMEM/F12 (1:1)	B27 w/o vitamin A N2 1 mM Glutamax	Epidermal growth factor (EGF; 10 ng/ml) Basic fibroblast growth factor (bFGF/FGF2; 10 ng/ml)	
Neural maturation medium (NMM)	Neurobasal:DMEM/F12 (1:1)	B27 w/o vitamin A N2 1 mM Glutamax Ascorbic acid (80 μM) db-cAMP (50 μM)	Brain-derived neurotrophic factor (BDNF; 10 ng/ml) Glial-derived neurotrophic factor (GDNF; 10 ng/ml)	

properties by providing cell protein–surface interactions, promoting cell adhesion, proliferation, and survival after the bioprinting process.

In addition to understanding how the structural and physical properties of the hydrogel affect both the bioprinting process and the microenvironment essential for cellular growth and function, we conducted rheological tests to characterize the mechanical properties of the Geltrex^{TM}/GelMA hydrogel and of the acellular constructs. Our goal was to investigate how the hydrogel stiffness and viscoelastic profile influence parameters such as extrudability and printing accuracy, as well as its impact on the mechanical strength and network structure of the 3D microenvironment.

We examined the hydrogel's flow behavior and apparent viscosity under continuous shear rate sweep by assessing the correlation between shear stress and shear rate. This experiment enabled us to simulate the hydrogel's deformation as it passes through the nozzle, changing from a bulk resting state to a high shear condition and its subsequent behavior once it reaches the print bed. Under applied stresses, the Geltrex^{TM}/GelMA hydrogel behaved as a non-Newtonian fluid with minimal thixotropy [Fig. 2(a)]. The apparent viscosity rheogram [Fig. 2(b)] revealed pseudoplastic behavior (typical of shear-thinning materials) and indicated the presence of yield stress, implying that the bioink remains stationary unless subjected to specific stress (e.g., pressing the syringe plunger) that exceeds the yield stress (Cooke and Rosenzweig, 2021). These features make the Geltrex^{TM}/GelMA composition suited for 3D bioprinting because pseudoplastic fluids exhibit reduced viscosity with increasing shear rates (i.e., during extrusion). Subsequently, post-extrusion, the hydrogel will quickly recover its original structure upon resting on the print bed instead of continuing to flow and spread due to its minimal thixotropy and a narrow hysteresis loop (Ferreira *et al.*, 2024).

We conducted an amplitude sweep for both the hydrogel and the 3D acellular construct [Fig. 2(d)] to set the linear viscoelastic region limit (LVE region), which establishes the range in which the test may be performed without compromising the integrity of the sample at a specified frequency (Herrada-Manchon *et al.*, 2023; Stojkov *et al.*, 2021). At 1 Hz, none of the samples exhibited a crossover point between the storage modulus (G') and the loss modulus (G''). The constant dominance of the storage modulus (G') over the loss modulus (G'') (i.e., $G' > G''$) implies that the samples display a gel-like or solid-like structure, defining them as viscoelastic solid materials (Herrada-Manchon *et al.*, 2023). Subsequently, the oscillatory frequency sweeps revealed that G' and G'' are dependent on the oscillation frequency [Fig. 2(e)]. At lower frequencies, the hydrogel exhibited solid-like behavior ($G' > G''$), characteristic of elastic materials; conversely, at higher frequencies, it presented liquid-like behavior ($G'' > G'$), qualifying it as a viscous material due to its fluid structure.

We employed G' values to assess the stiffness of the hydrogel before and after chemical gelation. Figure 2(g) illustrates the G' values acquired at a frequency of 1 Hz and a strain of 1%. Upon comparison of both samples, it is evident that, despite the hydrogel and the acellular 3D construct exhibiting elastic behavior, the photocrosslinking procedure promoted the formation of a more rigid/stiffer 3D architecture, with G' values exceeding those of the uncrosslinked hydrogel by more than tenfold (100 Pa).

Finally, due to the thermoresponsive nature of the hydrogel used, which consists of GelMA that solidifies at 10 °C and Geltrex^{TM} at 37 °C, we conducted a temperature ramp sweep to evaluate the hydrogel's behavior across a temperature range of 4–37 °C, aiming to identify the optimal printability window. Figure 2(f) illustrates that, up to 25 °C, the Geltrex^{TM}/GelMA blend exhibits elastic behavior; however, between 25 and 30 °C, the storage modulus declines while the loss modulus rises, nearing a point of crossing. Beyond 30 °C, the bioink restores its elastic properties as G' values grow. Similarly, the loss factor depended on temperature, with values surpassing 1 ($\tan\delta > 1$) from 23 to 27 °C, supporting the idea that the hydrogel functions as a viscous material in this range. Therefore, we suggest that the ideal printability range for this Geltrex^{TM}/GelMA composition is between 25 and 30 °C.

In addition to providing optimal mechanical strength for a 3D microenvironment, hydrogels used to mimic neural tissue must possess electrical conductivity, as a conductive matrix promotes cell proliferation and stimulation, potentially influencing neural network organization and neuronal morphology (Zhu *et al.*, 2019). The hydrogel we propose displays an electrical conductivity of 16.58 mS/cm at room temperature (data not shown), without the incorporation of metallic nanoparticles or other nanomaterials (Liang *et al.*, 2023), potentially facilitating neurite outgrowth and the differentiation and maturation of neural stem cells (NSCs) while also influencing their phenotypic orientation toward either neuronal or glial lineage.

Three-D bioprinted neurogenic niche-like structure: Cellular viability

After characterizing the physical and mechanical properties of the bioink, we conducted biological assays to investigate cellular viability, morphology, proliferation, differentiation, and motility within the 3D microenvironment of the bioprinted constructs. hNPCs were added to the hydrogel, bioprinted, and cultured in either neural expansion media (NEM; Table II) or NMM for up to 100 days (Fig. 3). The long-term culture shows that the Geltrex™/GelMA hydrogel holds chemical and mechanical properties to support key cellular events, such as survival and proliferation.

Because we were interested in generating a model mimicking the early development neurogenic niche, we focused on the first 40 days post-printing (dpp). We examined the 3D bioprinted neurogenic niche-like structure in three distinct periods: an early stage, corresponding to constructs from 5 to 10 dpp; an intermediate stage, from 17 to 23 dpp; and an advanced stage, from 28 to 36 dpp. The selected time frames were determined by periods in which self-organization was markedly different from previous stages. In the intermediate stage, we observed the formation of rosette-like structures [18 dpp, Fig. 4(a); 27 dpp, Fig. 4(b)], and in the advanced stage, we observed larger clusters [Figs. 4(c) and 4(d)] that were evident to the naked eye [Figs. 4(e) and 4(h)].

Over 30 days of post printing culture, there was an increase in cell proliferation and viability maintenance [Figs. 4(f) and 4(g)]. Although Alamar Blue measures cell viability, the increase in fluorescence intensity can also be interpreted as an increase in cell number due to proliferation. The distribution of live cells in the 3D constructs using the LIVE/DEAD assay shows a uniform pattern of viable cells (green), with a minimal presence of non-viable cells (red) [Fig. 4(g)]. These findings indicate that the printing process did not induce cell death over 30 days.

Three-D bioprinted neurogenic niche-like structure: Cellular differentiation

Interconnected clusters became apparent at the early stage (10–15 dpp), and the number and size of the clusters subsequently

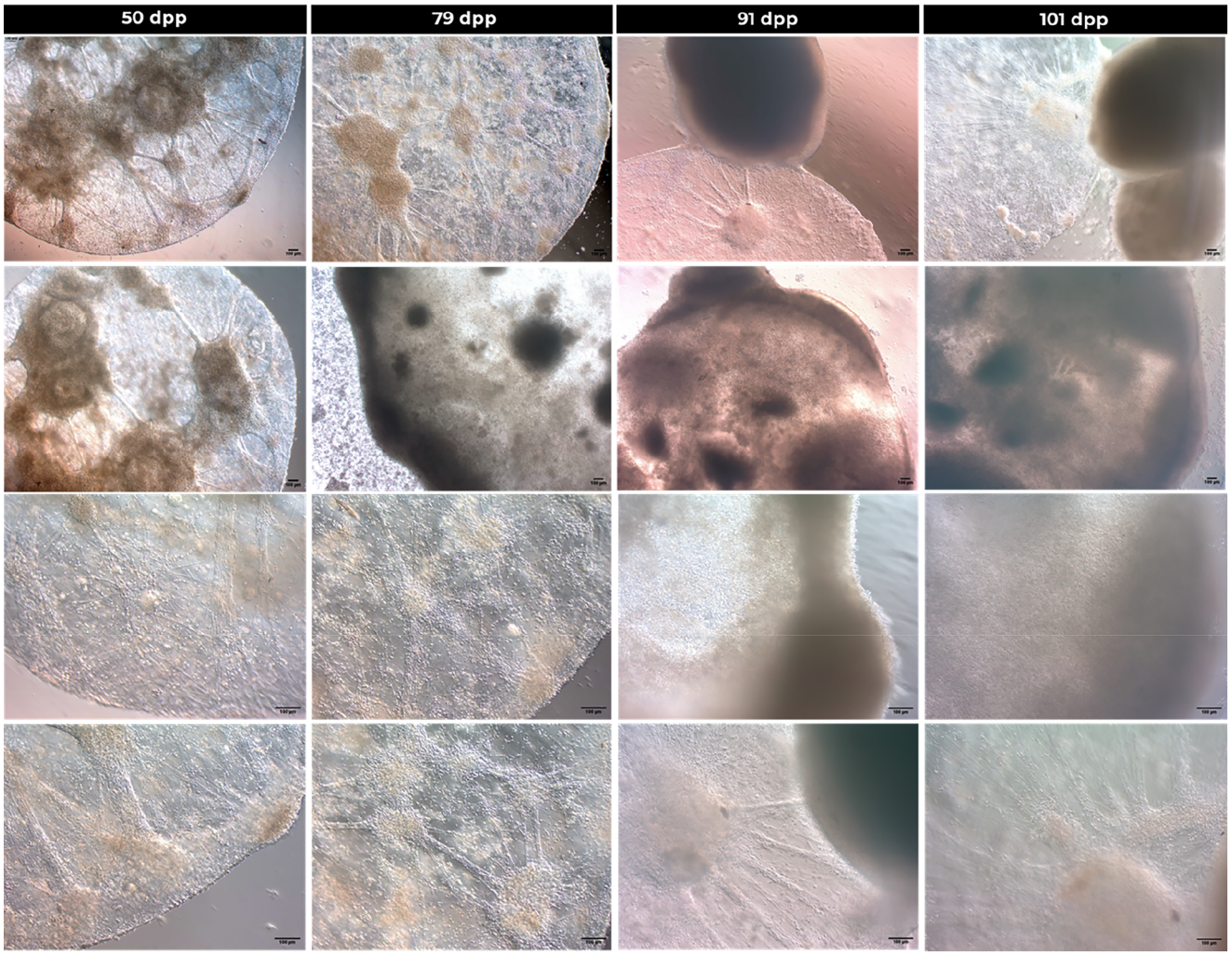

FIG. 3. 3D bioprinted hNPCs constructs after 50 days up to 101 days. Rows do not necessarily represent the same construct over time. Scale bar = 100 μm.

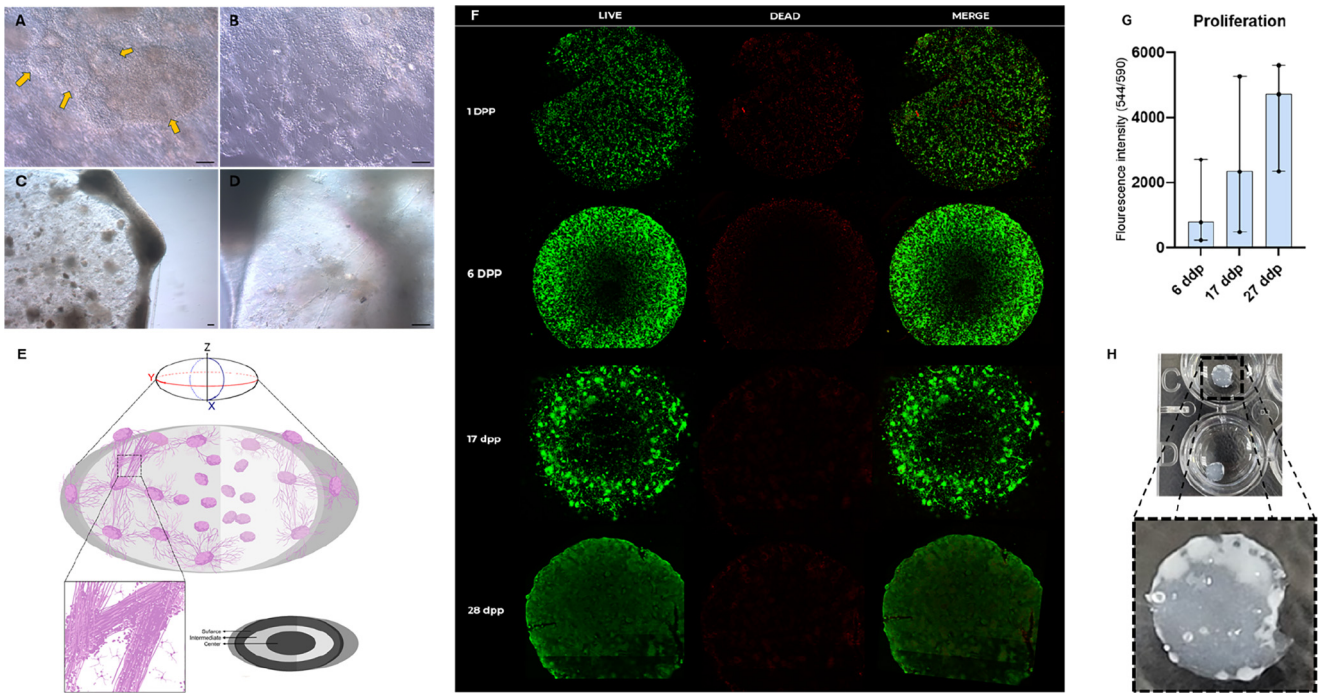

FIG. 4. Formation of a neurogenic niche-like structure by 3D bioprinted hNPCs. (a) Light microscope images of neural rosettes at 18 dpp. (b) Neural rosettes surrounded by neuron-like cells at 27 dpp. (c) and (d) Construct filled with cell clusters at 111 dpp in different magnifications. (e) Schematic illustration of the spatial distribution and interconnections of neurogenic niche-like structures within the 3D bioprinted construct. (f) LIVE/DEAD images of the whole construct (using the TileScan tool) at 1, 6, 17, and 28 dpp where green labels live cells and red the dead ones. Scale bar = 100 μm. (g) Proliferation analysis by Alamar Blue assay. Bars indicate median and 95% confidence intervals on fluorescence values. (h) Constructs in a 24-well plate at 60 dpp. Larger cell clusters are visible macroscopically as white dots.

increased. We hypothesized that each cluster represents a neurogenic niche-like structure in an early developmental stage and should have cells in different stages of differentiation, from proliferative hNPC/NSCs to neurons and astrocytes. The immunofluorescence assays showed cells expressing three specific markers for proliferation, neurons, and radial glial cells (Ki67, TUBB3, and FABP7, respectively) (Fig. 5) in constructs fixed at the three stages—although their spatial organization varied. Initially, cells were distributed across the construct without any discernible grouping or organization [Fig. 5(a) column]. During the transition to the intermediate stage, distinct clusters of FABP7$^+$ cells appeared, coinciding with denser regions of Ki67$^+$ cells surrounded by TUBB3$^+$ cells [Fig. 5(b) column].

When the constructs reached the advanced stage (>28 dpp), we observed organized structures connecting the clusters that could be visualized by light microscopy [Figs. 6(a) and 6(b); orange arrow in A]. We observed that the structures were formed mainly by processes from TUBB3$^+$ cells [Figs. 6(c) and 6(d)]. These structures will be referred to as "process bundles."

Upon closer examination of the cellular arrangements in the intermediate stage (21 dpp), it became evident that Ki67$^+$ proliferating cells were not exclusively confined to FAPB7$^+$ clusters (Fig. 7). We observed a difference in the structures formed at the construct's surface compared to those situated deeper within the construct's core. While cells in the top layers exhibit elongated processes connecting clusters, those closer to the core of the constructs, in deeper layers, were restricted to spherical formations composed of FABP7$^+$/Ki67$^+$ cells and devoid of TUBB3$^+$ cells, suggesting the formation of proliferative centers [Fig. 7(d) column].

Three-D bioprinted constructs cultured in NMM and NEM exhibited variations in the formation of cellular structures. In constructs maintained in NEM, NESTIN$^+$ cells were located in the periphery, while GFAP$^+$ cells were distributed throughout the whole construct [Figs. 8(a) and 8(b)]. NMM favored the formation of cell clusters with a limited presence of GFAP$^+$ cells [Figs. 8(c) and 8(d); supplementary material Fig. 1]. The main difference between NEM and NMM is the addition of growth and neurotrophic factors; NEM has epidermal growth factor (EGF) and basic fibroblast growth factor (bFGF), whereas NMM has brain-derived neurotrophic factor (BDNF) and glial-derived neurotrophic factor (GDNF).

Constructs cultured in NMM were analyzed for the expression of genes associated with maturation and critical neuronal development markers, MAP2 and FOXG1, and both genes were expressed throughout the 30 days (supplementary material Fig. 2).

Three-D bioprinted neurogenic niche-like structure: Cell migration

The presence of cell bodies throughout the process bundles, evidenced by immunofluorescence, suggested their potential role in supporting cell migration. In an initial time-lapse, we successfully

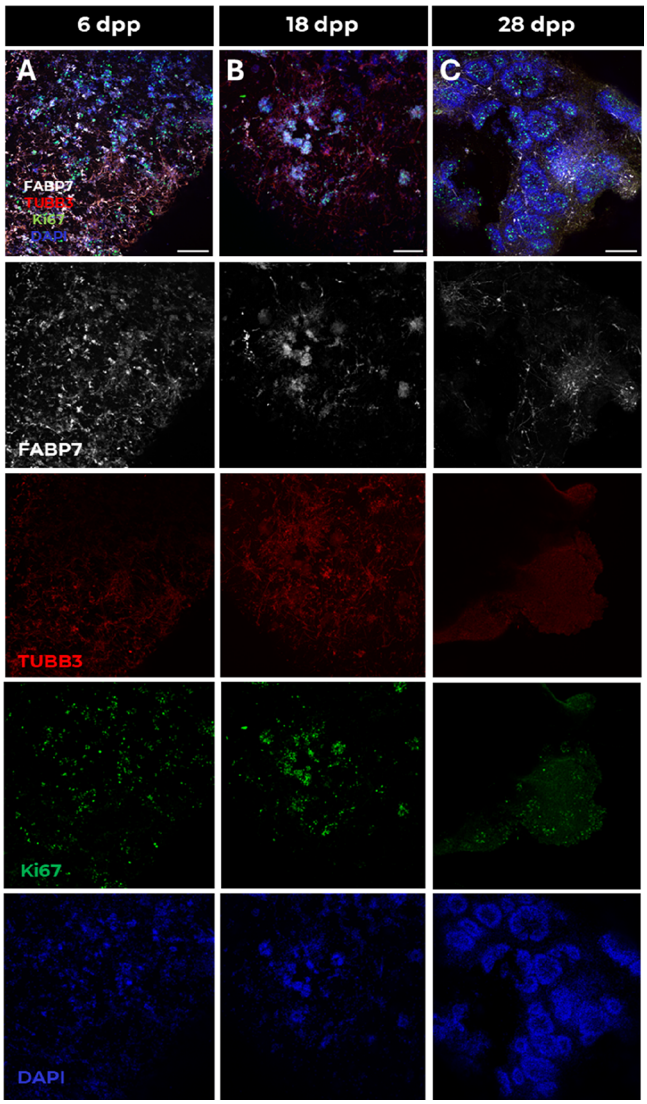

FIG. 5. Neurogenic niche-like structure formation on NMM at 6, 18, and 28 dpp. Immunofluorescence for Ki67, TUBB3, and FABP7 markers for proliferation, neurons, and radial glial cells, respectively. Column A: 6 dpp; Column B: 18 dpp; Column C: 28 dpp. Scale bar = 50 μm.

recorded the migration of an individual cell body, analogous to how the radial glia process facilitates neuroblast migration (supplementary material Fig. 3 and supplementary material Video 1). Subsequent investigation showed that cell mobility was not restricted to the intermediate stage or the process bundles as the cells crossed the construct independently of assistance from other structures (supplementary material Video 2). The movement persisted until 50 dpp, the final time point analyzed in this study (Fig. 9).

DISCUSSION

The human brain is a complex 3D structure comprising many cell types embedded within an ECM, significantly influencing their spatial distribution and function (Tarricone *et al.*, 2022). Challenges in investigating neural development *in vitro* include replicating the microenvironment and 3D architecture with a biomaterial that offers the physicochemical properties of the ECM, as well as scaffold properties that facilitate cell–environment interactions. These characteristics are crucial for achieving a functionality that 2D models lack, as their simplicity fails to adequately represent the intricate structure of the brain tissue, including how cells interact with physical and mechanical cues as signals and signaling modulators (Kitana *et al.*, 2024; Theus *et al.*, 2020). Concerning *in vitro* models of neurogenic niches, another critical factor during neural development is time, often regarded as the fourth dimension (4D) (Gao *et al.*, 2018; Theus *et al.*, 2020). In this study, we aimed to develop a 3D bioprinted structure that could be used to explore the early stages of human neurodevelopment *in vitro*.

We started this study by characterizing the Geltrex^{TM}/GelMA blend, which exhibits a desired behavior for creating hydrogels for 3D bioprinting. The rheological study identified the hydrogel as a viscoelastic solid that does not flow unless a deforming force is applied (shear-thinning behavior) but has a stiff consistency at rest (Figs. 1 and 2). Under this force, however, it flows as a liquid-like fluid because its viscosity decreases until it is at rest again, regaining its solid-like characteristics and its original shape and structure. The observed behavior is ideal for a bioink, as the hydrogel flows solely during the extrusion-based printing process when it passes through the bioprinter nozzle, likely due to the breakdown of physical crosslinks and the alignment of polymeric chains in the flow direction, thereby preventing any chain entanglements that could clog the nozzle (Chu *et al.*, 2023). Once it reaches the print bed, its internal structure is immediately reconstructed. The 3D architecture is maintained and reinforced by the chemical gelation process using UV photo cross-linking, ensuring it endures for extended periods of cell culture.

In addition to its impact on the bioprinting process, the physical and mechanical properties of the hydrogel also affect cellular survival and behavior. Optimal printability and gelation capacity are critical factors for bioinks intended for neural tissue culture, as the shear stress during extrusion can lead to cellular deformation, which is regarded as the primary contributor to cellular damage and death in 3D bioprinting. Although high-viscosity bioinks can help achieve shape fidelity, they also demand more pressure during printing, which increases shear stress. Consequently, low-viscosity materials that exhibit shear thinning behavior are essential for enhancing cell viability (Bercea, 2023; Gao *et al.*, 2018; Kitana *et al.*, 2024; Soltan *et al.*, 2019; and Theus *et al.*, 2020).

The hydrogel we developed also demonstrated positive outcomes regarding mechanically matching brain tissue characteristics. The brain is one of the softest tissues in the body, with an elastic modulus between 0.1 and 1 kPa (Sun *et al.*, 2018). Using G′ values for comparison, oscillatory tests indicated that our hydrogel exhibited storage modulus values within this range as a 3D model (~100 Pa). This means the bioprinted constructs provided cells with a substrate with enough softness for growth and process extension while maintaining sufficient rigidity to preserve the 3D microenvironment essential for network formation and spatial distribution. Substrate stiffness is a key cell fate determinant, influencing survival, proliferation, and differentiation. A softer matrix (<1 kPa) favors neuronal differentiation, whereas astrocytes prefer stiffer substrates and respond differently to

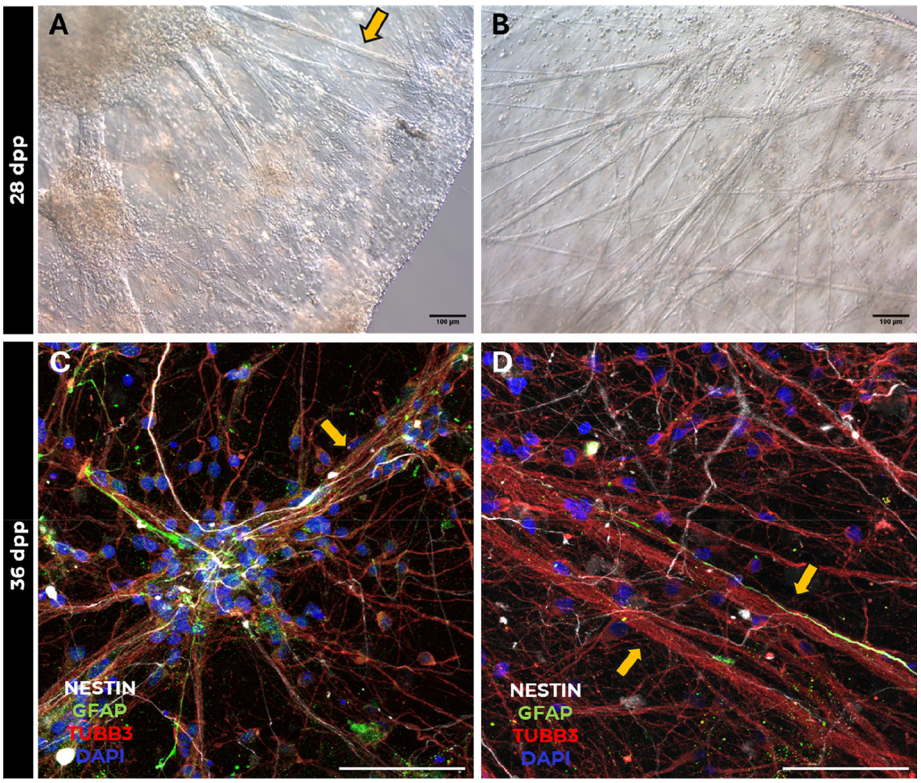

FIG. 6. Process bundles in bright-field and immunofluorescence microscopy of constructs cultured in NMM. Bright-field photos of constructs at 28 dpp (a) and (b). Immunofluorescence was performed in constructs at 36 dpp for NESTIN (white), GFAP (green), and TUBB3 (red) (c) and (d). Yellow arrows indicate process bundles. Bright-field scale bar = 100 μm; immunofluorescence scale bar = 50 μm.

variations in tissue mechanics (Engler *et al.*, 2006; Benincasa *et al.*, 2024; and Saha *et al.*, 2008).

Saha and colleagues created a hydrogel culture system composed of interpenetrating polymer networks to assess the impact of substrate stiffness on adult rat NSCs' behavior (Saha *et al.*, 2008). The authors reported that, in serum-free media, scaffolds with stiffness closely resembling the physiological stiffness of the brain (500 Pa) promoted the differentiation of NSCs into neurons, characterized by elevated expression of the neuronal marker TUBB3. In mixed medium differentiation settings using serum, softer gels (about 100–500 Pa) significantly benefited neuronal cultures, while stiffer gels (approximately 1–10 kPa) enhanced glial differentiation (Saha *et al.*, 2008). Similarly, Banerjee *et al.* investigated the impact of 3D alginate hydrogels, with elastic moduli ranging from 0.18 to 20 kPa, on the proliferation and differentiation of adult rat NSCs. The authors observed that the proliferation rate of NSCs diminished as the stiffness of the hydrogels increased. Furthermore, TUBB3 was significantly upregulated in the softest hydrogels (~180 Pa) with a comparable elastic modulus of the brain (Banerjee *et al.*, 2009).

Surface topography, particularly the presence of grooves or microgrooves, has also been shown to enhance cell adhesion, regulate morphology, accelerate migration, and promote neuronal differentiation (Cui *et al.*, 2021; Jahani Kadousaraei *et al.*, 2025; Lu *et al.*, 2016; and Sthanam *et al.*, 2019). Although the bioink did not exhibit porosity on SEM analysis, we observed that the presence of cells shifted its smooth surface into a complex, undulating structure, suggesting the substitution of the hydrogel components by cell-produced ECM. The fact that the acellular constructs lasted 28 dpp, whereas the cell-laden bioprinted constructs maintained their 3D structure for more than 100 dpp, indicates that the biomaterial is substituted by the ECM produced by the cells over time, promoting remodeling and maintenance of the 3D microenvironment as previously described by other works (Khetan *et al.*, 2013; Warren *et al.*, 2021). Acellular constructs are more susceptible to pH, temperature, and ionic composition than constructs containing cells (Lu *et al.*, 2024).

Madl and colleagues developed several hydrogels composed of elastin-like proteins with varying stiffness and degradability to determine how these parameters influenced the maintenance of adult murine NPCs stemness (Madl *et al.*, 2017). They discovered that, throughout a physiologically relevant stiffness range of approximately 0.5–50 kPa, the stemness of NPCs was independent of gel stiffness but substantially linked with hydrogel degradability. Degradability promoted cell-mediated ECM remodeling, thus enhancing the self-renewal and potency of the NPCs (Madl *et al.*, 2017).

According to the literature, GelMA and alginate are two of the most used hydrogels for 3D extrusion-based bioprinting, with alginate being predominantly utilized for 3D bioprinted neural models derived from hiPSCs (Fang *et al.*, 2023; Warren *et al.*, 2021). Both biomaterials exhibit good biodegradability and biocompatibility, with highly tunable physical and mechanical properties that may be modified by varying the concentrations of biopolymers and cross-linking agents, as well as their molecular weight, degree of substitution, and printing temperatures (Li *et al.*, 2024; Vorwald *et al.*, 2020). Their main distinction is that, although GelMA hydrogels usually have poor printability at low concentrations (<5%) for extrusion-based 3D printing, they offer advantageous biochemical features that are absent from alginate

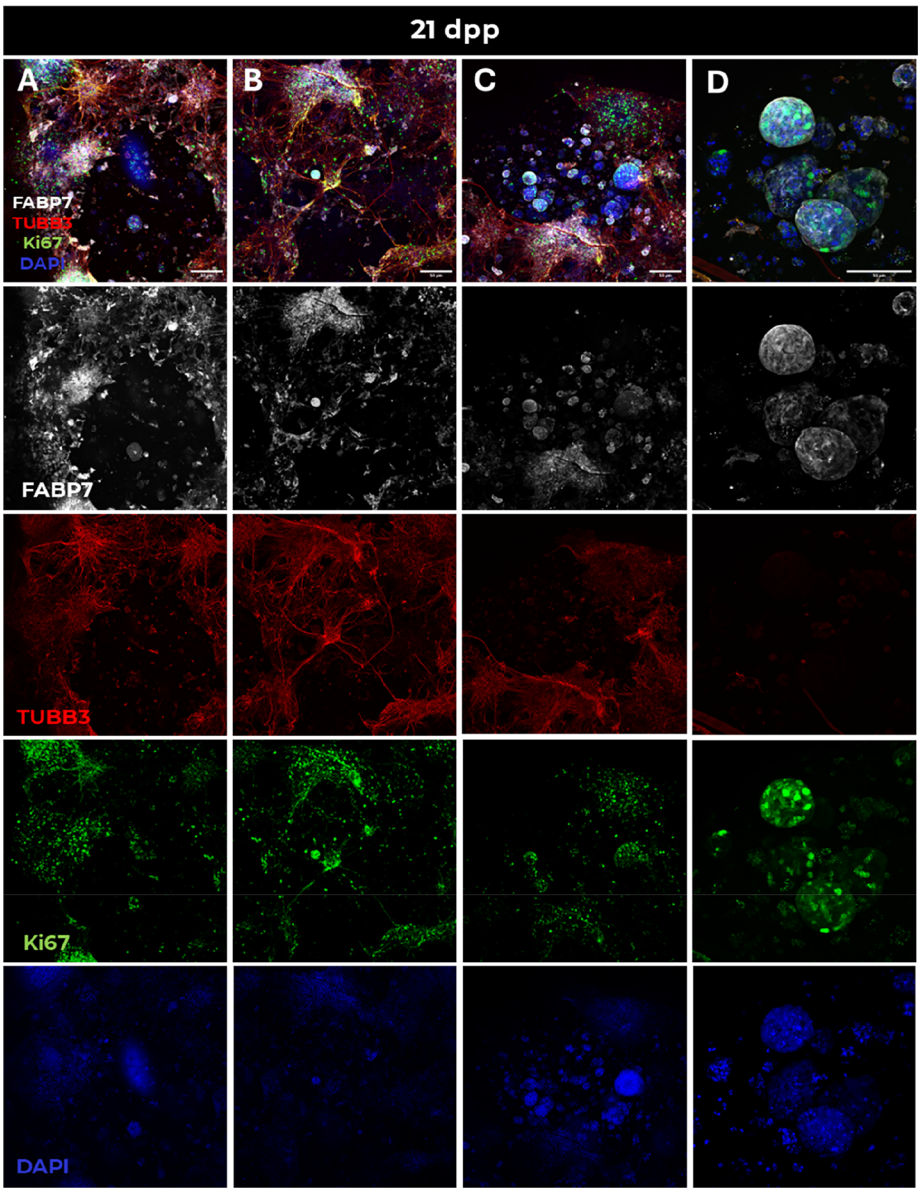

FIG. 7. Neural niche-like structure formation on NEM at 21 dpp. Immunofluorescence for Ki67, TUBB3, and FABP7 markers for proliferation, neurons, and radial glial cells, respectively. Cells on superficial layers of the construct form cell clusters interconnected by process bundles and can differentiate into neurons and form neural rosettes (a) and (b). In some regions, it is possible to see cells at the surface (a and b rows) and cells closer to the construct's core (c) and (d) simultaneously. Different focuses in the Z-axis favor cells at the construct core in greater magnification, and they remain spherical with no neurites or surrounding neurons (d). Illustration in Fig. 4(e) shows "surface" and "center" locations in the construct. Scale bar = 50 μm.

hydrogels, including matrix–metalloproteinase (MMP)-sensitive degradation sites and cell attachment-promoting properties due to the presence of the cell-binding tripeptide Arg-Gly-Asp (RGD) sequence (Fu *et al.*, 2024; Li *et al.*, 2024). The use of Geltrex™ for 3D brain modeling is uncommon; rather, Matrigel® (another commercial ECM mixture), is the most employed natural ECM extract for 3D bioprinting and organoid generation (Chen *et al.*, 2023). However, because of its thermoresponsive properties, a hydrogel composed solely of Matrigel® is more challenging to bioprint without regulating the process temperature, as it is liquid at 4 °C and becomes a gel at 37 °C. Consequently, it has been utilized with polymers that exhibit adjustable mechanical properties (Alave Reyes-Furrer *et al.*, 2021; Xiaorui *et al.*, 2023).

Considering these data, the Geltrex™/GelMA blend we developed effectively minimizes the limitations of using either biomaterial independently. The hydrogel composition enabled us to 3D bioprint constructs that sustained hNPC survival, proliferation, and differentiation over extended periods (Fig. 3). We also observed cell mobility (Fig. 9; supplementary material Fig. 2 and Videos 1 and 2), neurite extension, and self-organization across cells with distinct phenotypic profiles (Figs. 4–8).

Regarding the factors that influence cell viability in 3D printing (e.g., timing, biomaterial composition, cell type, cell density) (Warren *et al.*, 2021), studies have reported bioprinting-related methods that sustained hNPCs and/or cells matured from hNPCs from 4 to 40 days (Bilkic *et al.*, 2022; Joung *et al.*, 2018; Sharma *et al.*, 2020; and

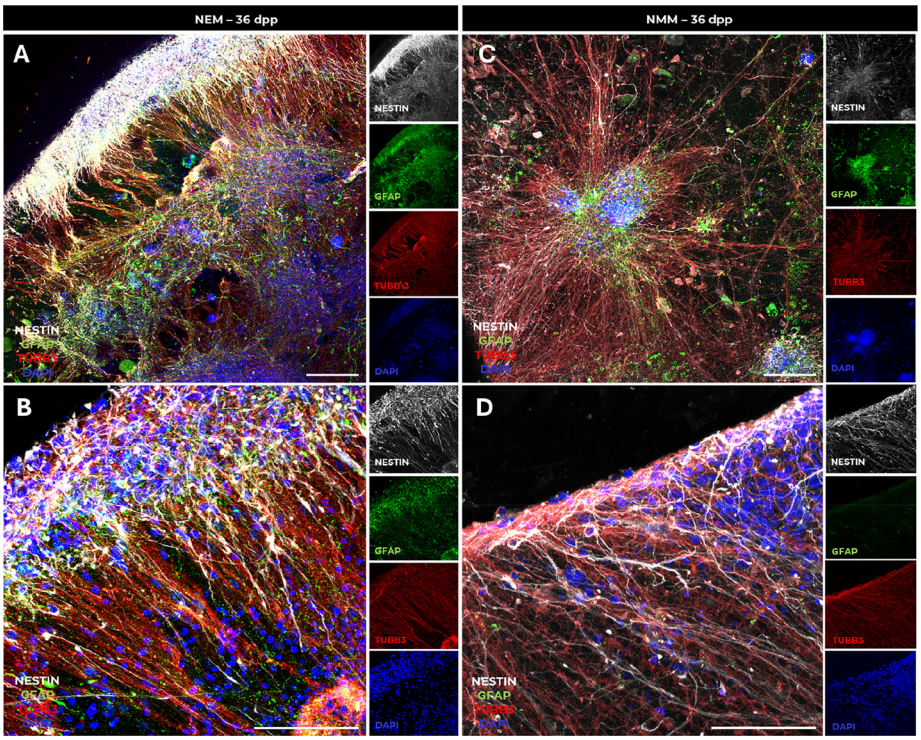

FIG. 8. Immunofluorescence at 36 dpp of 3D bioprinted hNPCs cultured in neural expansion medium (NEM) (a) and (b) or maturation medium (NMM) (c) and (d). NESTIN (white) and GFAP (green) are hNPC markers, and TUBB3 (red) is a marker for mature neurons. Scale bar = 50 μm.

Yan *et al.*, 2024). The Geltrex™/GelMA blend could sustain the various cellular events for 111 days. However, we limited most of our analysis to the first 36 days. During that time, cells survived the printing protocol and remained viable, as shown in the LIVE/DEAD assays (Fig. 4). The mean values obtained from the proliferation analysis suggest a difference between the timepoints analyzed, although not statistically significant, likely due to variability and heterogeneity among constructs, highlighting the need for a larger sample size. Even so, cell

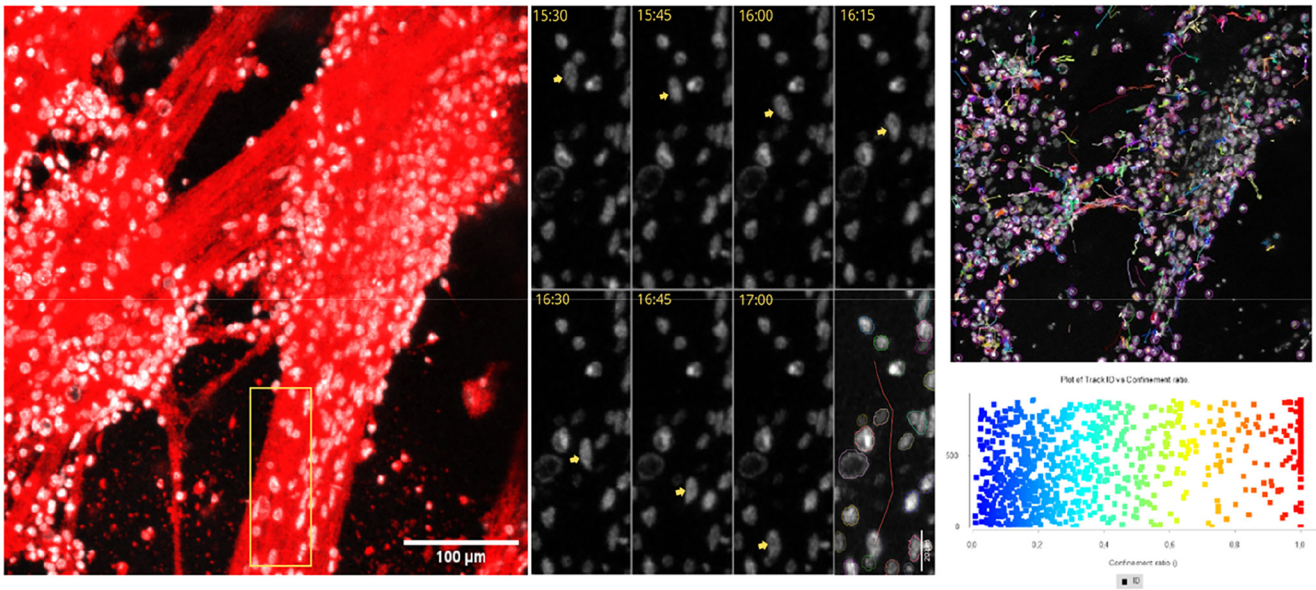

FIG. 9. Time-lapse confocal microscopy analysis. Cell movement was observed with CellTracker™ Red CMTPX Dye and Hoechst nuclei staining at 50 dpp with captures taken in 15-min intervals. Scale bar = 100 μm. After Drift Correction (Fiji plugin) nuclear migration was analyzed using the TrackMate plugin in Fiji/ImageJ, employing a Laplacian of Gaussian (LoG) detector and Linear Assignment Problem (LAP) tracker. The plot shows the confinement ratio for individual tracks: values close to 0 represent confined or random movement, while values approaching **1** indicate directed motion along a consistent orientation.

proliferation support of this bioink was observed by light microscopy and immunofluorescence as cell clusters were formed, continuously grew, cells spread out over the construct's area, and were positively stained for Ki67 (Fig. 5).

In our previous publication (Cruz *et al.*, 2023), we demonstrated that the model presented in this paper enables cells to exhibit their expected behaviors, including the acquisition of NPC-like morphology, positive staining for GFAP and NESTIN, the extension of processes, and the ability to self-organize. In the present study, we identified by immunofluorescence that the cell clusters were predominantly positive for GFAP, NESTIN, and FABP7 (Fig. 7). Notably, the spatial distribution of the cells is not homogeneous, where there were regions and cells seemingly positive for none, one, and even all the markers, displaying diverse cellular profiles. Heterogeneity might reveal the dynamic and temporal aspects of development, an essential dimension of neurodevelopment (Giachino *et al.*, 2014; Liour *et al.*, 2006). This change in the staining pattern was observed in the constructs over time during this study. Around 20 dpp, cell clusters were formed and had a noticeable concentration of $Ki67^+$ cells, a known proliferation marker. In many constructs, neural rosettes were present. At 36 dpp, constructs cultured in both NEM and NMM had positive cells for the progenitor markers; neural rosettes were still observable in some constructs (Fig. 4), but the staining pattern was distinct.

The presence or absence of GFAP in $NESTIN^+$ cells indicates how close the cells are to an NSC identity or to a more advanced status in maturation, where $NESTIN^+/GFAP^+$ cells are early progenitors that become less present in the adult neurogenic niche (Fukuda *et al.*, 2003). We observed that the constructs cultured on NEM displayed abundant $NESTIN^+/GFAP^+$ cells by 36 dpp, suggesting the presence of early progenitors. Constructs maintained in NMM displayed fewer $NESTIN^+/GFAP^+$ cells, limited to cell clusters. In contrast, the rest of the construct contained cells positive for late progenitors ($NESTIN^+/GFAP^-$) and neurons ($TUBB3^+$), indicating a maturation process. Thus, constructs maintained in NEM had more $NESTIN^+$ co-stained with GFAP, while NMM showed minimal GFAP co-staining, corroborating the possibility of the cells being at different maturation stages (Fig. 8).

Much of cell behavior in the neurogenic niche is regulated by the uptake or release of soluble factors in the microenvironment (e.g., FGF, BNDF, GNDF), some of which are produced by the cells in the niche (Andreotti *et al.*, 2019; Willis *et al.*, 2022). The two components of NEM that are not present in NMM are EGF and basic fibroblast growth factor (bFGF), which stimulate survival, proliferation, maintenance of differentiation potential, and migration of NPCs (Li *et al.*, 2022; Regalado-Santiago *et al.*, 2016; Supeno *et al.*, 2013; Sutterlin *et al.*, 2013; and Douet *et al.*, 2013). EGF increases cell proliferation of the heterogeneous population of $FABP7^+$ NSCs in postnatal and adult neurogenic niches (Giachino *et al.*, 2014). The combination of EGF and bFGF could explain the presence of early progenitors in constructs cultured in NEM. Interestingly, cells across the surface of all constructs expressed TUBB3, a microtubule protein expressed by mature neurons. $TUBB3^+$ neurons were generated when the constructs were cultured in NEM, suggesting the induction of neuronal maturation. EGF and FGF behave differently *in vivo* and have been associated with promoting neural differentiation in neurogenic niches *in vivo* and explants, suggesting that our model may also display some of the *in vivo* characteristics (Kuhn *et al.*, 1997; Lamus *et al.*, 2020; and Li *et al.*, 2022). BNDF and GDNF are neurotrophins that promote neuronal differentiation, branching, neurite formation, and synapse maturation (Khazaei *et al.*, 2020; Wu *et al.*, 2016; and Wakeman *et al.*, 2014). Signs of maturation of cells in constructs cultured in NMM were observed by immunofluorescence. In addition, we analyzed the gene expression of MAP2 and FOXG1, markers for mature neurons and associated with telencephalon/forebrain patterning, respectively (supplementary material Fig. 1). FOXG1 is expressed in neurogenic niches during neurodevelopment and in adult neurogenic niches (Schaffner *et al.*, 2023). The early detection of MAP2 at 5 dpp reinforces the heterogeneity of the constructs, suggesting the presence of cells simultaneously at different stages of maturation. While it is expected MAP2 to increase over maturation and FOXG1 to increase during NPCs induction from hiPSC but decrease during maturation (Hettige *et al.*, 2022, 2023; Vagaska *et al.*, 2020; and Yan *et al.*, 2024), over the period analyzed, the expression of both genes was detected; however, no statistically significant changes were observed. Some possible reasons for that are the continuous growth of the progenitor clusters and the heterogeneous population at different stages of maturation combined with the variation amongst constructs. The heterogeneity may mask the increase in gene expression of maturation markers. Also, it is difficult to detect differences through bulk RNA extraction and quantitative PCR (qPCR) analysis. Techniques such as single-cell or single-nucleus RNAseq would be more sensitive. However, optimizing those protocols in 3D constructs has been challenging (Wang *et al.*, 2018). These features demonstrate how this proposed model may be used for multiple purposes by favoring different characteristics when responding to the specific soluble factors and morphogens added to the media.

Conventional 2D and 3D culture methods may allow for the formation of cell–cell networks and facilitate neurite growth, but are limited in reproducing the connections by process bundles. A few examples in the literature are the use of a complex hemicylindrical microchannel array system, in which fetal rat cortical NPCs could form neural spheroids that secreted ECM and were interconnected by $TUBB3^+$ process bundles (Jeong *et al.*, 2015) and hNSC cultured in a Matrigel® and collagen 3D scaffold that clustered and created a network of $TUBB3^+$ processes (Vagaska *et al.*, 2020). In the 3D bioprinted model we developed, long $TUBB3^+$ process bundles emerged from the self-organized hNPCs clusters, creating a network that supports cell migration and communication among clusters. TUBB3 was not limited to the process bundles, also known as axonal tracks; individual $TUBB3^+$ neurons increasingly populated the construct and extended their processes (Figs. 6 and 8).

During neurodevelopment and in adult neurogenic niches, immature neurons (neuroblasts) migrate away from their birthplace. In embryonic development, neuroblasts use radial glia as a scaffold to reach their cortical position, and in the subventricular zone neurogenic niche in adults, neuroblasts migrate toward the olfactory bulb using chain migration in which they use each other as support following a glial tube as guidance (Jinnou *et al.*, 2018; Nadarajah *et al.*, 2001; and Paredes *et al.*, 2016). In our model, we observed cells migrating on the surface of the process bundles that serve as support and cells migrating without using the processes as support (Fig. 9; supplementary material Fig. 2; supplementary material Videos 1 and 2).

The current approaches used to recapitulate characteristics of neurogenic niches are transwell co-cultures, cortical organoids, and 3D bioprinting. Transwell offers a variety of options for seeding different

cell types with customizable materials, such as membranes made from various materials and a range of pore sizes. Vascularized NSC niche models have been produced, but due to structure limitations, they cannot recapitulate the spatial complexity of a 3D environment as other models (Shin *et al.*, 2014; Wang *et al.*, 2017). Cortical organoids allow cells to self-organize in a complex 3D manner with variable region-specific identities, migration, neurogenesis, laminar formation, and many human-specific neurodevelopmental features (Andrews *et al.*, 2020, 2022; Huang *et al.*, 2021; and Kadoshima *et al.*, 2013). Some of the difficulties regarding this approach are the long time required, reproducibility, lack of vascularization that promotes cell death as the organoid grows. Some aspects of cell behavior (e.g., migration) are better studied with more complex techniques such as assembloids, fusion, connection, and polarization (Huang *et al.*, 2021; Jensen and Little, 2023; and Lee and Sun, 2022). For 3D bioprinting, hydrogels provide versatility to better mimic region-specific ECM, particularly in tuning mechanical and rheological properties to match tissue-specific requirements. Hydrogels can be tunable for specific applications by promoting different cell behaviors (Xu *et al.*, 2021; Lo *et al.*, 2000). Printing is fast, low-cost, and widely available. Still, each biomaterial requires a different printing technique, which can cause undesirable effects on the cells, such as high compression that can damage the cell membrane during printing. Additionally, depending on the material and printing method, the resolution is limited, making it difficult for cell positioning (Kacarevic *et al.*, 2018). Studies combining techniques to mitigate shortcomings and optimizing qualities such as speed, definition, tunability, and scalability, leading to the formation of complex structures, shall overcome the present difficulties.

Limitations of this study

Although the Geltrex^{TM}/GelMA blend increased swelling rates over time, which indicated it absorbs culture media and diffuses nutrients throughout the construct, it also demonstrated high hydrophilicity, which gave the gel minimal surface tension. These features and the hydrogel's softness (storage modulus ranging from 10 to 100 Pa for the hydrogel and bioink, respectively) enabled us to simulate a brain-like microenvironment, albeit with the difficulty of maintaining an accurate 3D design.

Concerning cellular behavior within the construct, cells nearer to the surface exhibited increased proliferation (as indicated by Ki67 staining) and more neural projections than those in the construct's core. One alternative to overcome these obstacles is to modify the hydrogel's mechanical strength and stiffness by changing its composition or the concentration of photoinitiator. However, since those alterations may affect the bioink's properties, a new characterization will be required.

Our model does not enable orientation for maturing neurons as it relies on self-organization. All constructs exhibited similar overall characteristics over time, but variation was observed among them. We hypothesize that the variation was the leading cause for the lack of statistical significance in the proliferation assay and qPCR analysis. Additionally, the increase in clusters may favor detecting genes from more proliferative cells, which are in higher numbers, masking the genes expressed by cells in advanced maturation stages when analyzing bulk RNA. Single-cell RNAseq might be more appropriate for analyzing gene expression profiles, but recovering single cells from the constructs is still challenging.

CONCLUSION

Our results show that the Geltrex^{TM}/GelMA blend created a dynamic environment that can recapitulate aspects of neurodevelopment. Our findings indicate that the bioink provides a suitable microenvironment for cell survival, proliferation, differentiation, and migration. The complexity of the structures formed resemble neurogenic niches, and this was possible because cells were viable for more extended periods than other reported 3D bioprinting protocols, reaching more than three months in culture. The clusters predominantly comprise proliferating hNPCs, with radial glia being a key component. The hNPCs proliferated within the clusters, and cells could move using the process bundles as scaffolds or migrate without the support of the bundles. Simultaneously, cells matured and differentiated into TUBB3^{+} neurons, displaying the temporal aspect of neural development. We propose this as a 4D model to study the key cellular and molecular features of neurogenic niches, including time as the fourth dimension.

METHODS

Human-induced pluripotent stem cell (hiPSC) culture and differentiation into neural progenitor cell (hNPC)

The human-induced pluripotent stem cells (hiPSCs) were kindly provided by Professor Lygia V. Pereira from the National Embryonic Stem Cell Laboratory (LaNCE), in São Paulo, Brazil. Blood erythroblasts were reprogrammed by episomal factors containing the Yamanaka factors Oct3/4, Sox2, cMyc, and Klf-4. Their karyotype was analyzed, and no abnormalities were found. The iPSCs were cultured in a six-well plate coated with Geltrex^{TM} in Essential 8 (E8) medium, which was changed daily. Cells were passed when they reached approximately 80% confluence using 0.5 M EDTA solution, until they were subjected to the neural progenitor cell (NPC) differentiation protocol.

At passages 18 and 23 dual SMAD inhibition was used to generate the hiPSC-derived NPC (Andrews and Kriegstein, 2022; Bose *et al.*, 2021; Chambers *et al.*, 2009; de Jongh *et al.*, 2022; de la Vega *et al.*, 2019; Hofer and Lutolf, 2021; and Kim *et al.*, 2020). Cells were detached when the confluency was high enough so that they would reach 100% confluency the next day and seeded onto Geltrex^{TM}-coated wells. In the next day, E8 was replaced by neural induction media (NIM; Table II) consisting of 50% Neurobasal Medium and 50% DMEM/F12 supplemented with B27 without vitamin A, N2, 1 mM Glutamax, 0.1% PS, SMAD LDN193189 (0.1 μM) and SB431542 (10 μM). Medium was changed daily until Day 14, when cells were passaged with StemPro Accutase onto six-well Geltrex^{TM}-coated plates. Then, cells were cultured with neural expansion media (NEM; Table II), similar to NIM however without the SMAD inhibitors and with the addition of non-essential amino acids and growth factors, 10 ng/ml of epidermal growth factor (EGF), and 10 ng/ml basic fibroblast growth factor (bFGF). NEM was changed every other day, and cells were passaged when needed with StemPro Accutase.

The hiPSC-derived NPCs were successfully generated and confirmed by the increase in expression and presence of hNPC-related markers by immunofluorescence and qRT-PCR and a decrease in pluripotent-related markers, as described in a previous publication from our group (Cruz *et al.*, 2023).

Hydrogel preparation

The bioink composition and preparation were also previously described by our group (Cruz *et al.*, 2023). Briefly, gelatin methacrylate (GelMA) was synthesized via the direct reaction of gelatin (*MW*: ∼50 to 100 kDa; Type A, porcine skin; *gel strength*: ∼300 g Bloom) with methacrylic anhydride in phosphate-buffered saline (PBS, pH 7.4), following the protocol previously established by our group (de Melo *et al.*, 2021). An 8% (w/v) GelMA solution was prepared in PBS, and 0.5% (w/v) of the photoinitiator Irgacure was added, yielding a final concentration of 0.25% after mixing with Geltrex™.

The solution was incubated overnight at 37 °C, protected from light. If not used within 24 h, it was stored at 4 °C for up to 7 days. Before use, the solution was incubated at 37 °C until fully liquefied and homogeneous, then filtered through a 0.22-μm polypropylene filter. Finally, the 8% GelMA solution was mixed at a 1:1 volume ratio with Geltrex™—a reduced growth factor basement membrane matrix, similar in composition to Matrigel™, but with different proportions of constituents—resulting in a 4% GelMA-based bioink.

3D bioprinting of hNPCs and maturation

The 3D bioprinting protocol was adapted from a previous study by our group (Cruz *et al.*, 2023), with minor modifications, based on the method previously described (de Melo *et al.*, 2021). Bioprinting was performed using a 3DBS Educational Starter Printer with G-code commands. The bioink was extruded from a 5 ml syringe at an average printing speed of 3.3 mm/s, using a 22 G needle (25 mm length, 7 mm outer diameter, 0.413 mm inner diameter). Before printing, UV light (0.69 mW/cm^2) was activated for at least 5 min to ensure optimal cross-linking conditions. hiPSC-derived neural progenitor cells (hNPCs) were resuspended in the bioink at a density of 12–15 × 10^6 cells/ml. Constructs (measuring 4 × 4 × 0.6 mm) were bioprinted in a culture dish placed on top of a recyclable ice pack to promote physical gelation. Following the printing process, the constructs underwent exposure to UV light for 5 min at room temperature to finalize the chemical gelation through the photocrosslinking process. Subsequently, the constructs were placed onto 24-well culture plates and maintained in either NEM or neural maturation medium (NMM; Table II) at 37 °C with 5% CO_2. The NMM formulation consisted of 50% Neurobasal and 50% DMEM/F12, supplemented with B27 without vitamin A, N2, 2 mM Glutamax, 0.1% penicillin–streptomycin (PS), ascorbic acid (80 μM), db-cAMP (50 μM), 20 ng/ml brain-derived neurotrophic factor (BDNF), and 10 ng/ml glial-derived neurotrophic factor (GDNF). Medium changes were performed every two days for NEM and every three days for NMM.

Microstructure analysis

The bioprinted constructs were examined using scanning electron microscopy (SEM) Zeiss, USA, EVO MA-10, operating at a voltage of 20 kV. Samples were observed after 36 days in culture with NMM at 37 °C with 5% CO_2. To prepare for SEM, the constructs were dehydrated using a sequential series of acetone solutions (30%, 50%, 70%, and 100%) for 5 min each. Subsequently, they were immersed in a mixture of acetone and hexamethyldisilazane (HMDS) in a 1:1 ratio for 5 min, followed by HMDS alone until complete evaporation. The dried constructs were then sputter-coated with a thin layer of gold prior to SEM observation.

Wettability

The wettability of the hydrogel, defined as its capacity to sustain contact at a specific contact angle with solid surfaces such as the nozzle and print bed, was assessed using the sessile drop method with 3 μl water droplets applied to the surface of the construct. Wettability, degradation, swelling, and rheological experiments were performed using acellular constructs, circular 3D hydrogels created by depositing bioink into circular molds and photocrosslinking for 5 min at room temperature. Images of a single de-ionized water droplet on the construct's surface were captured at 2-min intervals using a Goniometer (KRUSS, Germany, EasyDrop DSA 100S) equipped with a charge-coupled device (CCD) camera. The initial contact angle was measured 5 s after drop deposition to allow the droplet to reach equilibrium. Measurements were performed in triplicate on different constructs. All experiments were conducted under controlled conditions, maintaining a temperature of 25 ± 3 °C and a humidity level of 50% ± 10%. Contact angle calculations were performed using the open-source software ADVANCE.

Hydrogel degradation rate

The degradation rate was evaluated to determine the material's stability following its chemical gelation. To do this, immediately after photocrosslinking, the acellular constructs were weighed (initial dry weight, *Wd0*) and submerged in PBS (pH 7.4, 10 mM) at 37 °C for various time points: 1, 2, 7, 18, and 28 days. After each period, the samples were weighed (final wet weight, W_f), gently placed on filter paper for 10 min at room temperature and reweighed with a scale accurate to 0.0001 g (final dry weight, Wd_f). Nine samples were analyzed for each timepoint. Mass loss at different timepoints was determined using the following equation:

$$Degradation\,(\%) = \frac{Wd_0 - Wd_f}{Wd_0} \times 100.$$

Hydrogel swelling degree

Similarly to the degradation test, the acellular constructs were weighed immediately after the chemical gelation process. Then, they were incubated in PBS (pH 7.4, 10 mM) at 37 °C for 1, 2, 7, 18 and 28 days. At each timepoint, nine samples were weighed as described previously. Swelling percentage was calculated using equation, as follows:

$$Swelling\,(\%) = \frac{W_f - Wd_0}{Wd_0} \times 100.$$

Hydrogel rheological characterization

The mechanical properties of both the bioink and acellular constructs, also referred to as the 3D model, were evaluated through rheological measurements on a stress-controlled rheometer equipped with a parallel-plate setup (25 mm diameter, 200 μm gap). Flow behavior and viscosity were assessed by applying shear rates from 0.01 to 100/s and back, allowing a 30-s interval between each set of measurements. Subsequently, oscillatory tests were performed to determine the viscoelastic properties of the hydrogels and constructs. During amplitude sweeps (1 Hz, 0.1%–100% strain) and frequency sweeps (1% strain, 0.1–10 Hz), the storage modulus (G′), loss modulus (G″), and loss

TABLE III. Primers' sequences. GAPDH: Glyceraldehyde 3-phosphate dehydrogenase, ACTB: Beta-actin, MAP2: microtubule-associated protein 2, FOXG1: Forkhead box G1.

Gene	Sequence	Forward	Reverse
GAPDH	NM_001256799.3	GTGGTCTCCTCTGACTTCAAC	CCTGTTGCTGTAGCCAAATTC
ACTB	NM_001101.5	TCCACGAAACTACCTTCAACTC	CAGTGATCTCCTTCTGCATCC
FOXG1	NM_005249.5	GCCAGCAGCACTTTGAGTTA	TTGTTGCCCTGCATGTTATTG
MAP2	NM_001039538.2	TGGTGCCGAGTGAGAAGAAG	AGTGGTTGGTTAATAAGCCGAAG

tangent (tan δ) were recorded. Unless otherwise indicated, all experiments were conducted at 25 °C in triplicate, and the rheograms presented represent the mean of these three measurements.

Hydrogel electrical conductivity measurements

Electric conductivity was assessed using a conductivity meter (LACTEA BRAZIL). Both 8% GelMA solution and pure Geltrex™ were measured individually, and the Geltrex™/GelMA hydrogel.

Cell viability and proliferation in bioink

Cell viability was assessed using the LIVE/DEAD™ Cell Imaging Kit, according to the manufacturer's instructions. A construct was selected and incubated for 20 min at room temperature in a 1:1 ratio of the Live/Dead solution and maturation medium. Photos were acquired using the tiles that function in the Leica DMI6000 or confocal Zeiss LSM 780 microscope.

Proliferation was assessed by the Resazurin assay according to the manufacturer's instructions. Three bioprinted constructs for each timepoint were moved to a well of a 24-well plate containing 500 μl of a 10% Resazurin solution diluted in maturation medium. Samples were incubated in the dark for 4 h at 37 °C and 5% CO_2. A single cell-free construct per time point without cells was simultaneously incubated in Resazurin solution (negative control). Subsequently, 100 μl of the solution of each sample was transferred to a new 96-well plate for fluorescence measurement using the plate reader SpectraMax®M3 (Molecular Devices, USA).

Immunofluorescence analysis

For immunofluorescence analysis, the constructs were washed with PBS, 10 mM, pH = 7.4, for 5 min and then fixed with 4% paraformaldehyde for 40 min. They were washed three times with PBS for 5 min each once more, followed by an incubation with 0.1 M glycine solution for 15 min. After repeating the three washes, samples were blocked for 1 h with 5% (v/v) normal goat serum in PBS containing 0.1% Triton X-100. Then, they were incubated with the following primary antibodies overnight: FABP7, NESTIN, GFAP, TUBB3, or Ki67. Samples were then washed with PBS three times and then incubated with DAPI and the following secondary antibodies (1:500) for 2 h: AlexaFluor 488, AlexaFluor 594, or AlexaFluor 647. The samples were analyzed using confocal microscopy (Confocal Zeiss LSM 780 and Leica TCS SP8 CARS).

RT-qPCR analysis

RNA extraction was carried out utilizing TRIzol™ reagent, while cDNA synthesis was obtained by the Super-Script™ III First-Strand Synthesis Super-Mix, following the manufacturer's instructions. The primer sequences are detailed in the following table (Table III). Quantitative PCR (qPCR) analysis utilized Fast SYBR™ Green Master Mix. Relative expression levels were determined using the $2^{-\Delta\Delta Ct}$ method, employing the geometric mean of two endogenous genes (beta-actin and GAPDH) as internal reference controls.

Cell movement analysis

Cell movement capability post-printing was evaluated through time-lapse confocal microscopy analysis. The constructs were incubated with CellTracker™ Red CMTPX Dye and NucBlue™ Live ReadyProbes™ Reagent (Hoechst 33342) for 45 min, washed 3× in DMEM, and imaged in the Confocal Zeiss LSM 780 microscope. Cell movement was observed for a maximum of 48 h, with captures taken in 15-min intervals.

Directionality was evaluated using the Trackmate plugin in Fiji/ImageJ. The confinement ratio tells how "efficient" was a displacement in getting far away from its starting point. It is defined as the net-displacement divided by the total distance. The net-displacement is given by the "track displacement" feature, and the total distance is given by the "total distance traveled" feature. The confinement ratio is a unitless value that ranges from 0 to 1. Values close to 0 indicate a confined movement, where the particle (cell) stays close to its starting point. Values close to 1 indicate that the particle (cell) travels along a line with a constant orientation.

Statistical analysis

The data were analyzed using GraphPad Prism 9.0 (GraphPad Software, San Diego, CA, USA) and depicted as means with standard deviation (SD). Treatment groups were assessed via one-way analysis of variance (ANOVA), supplemented, if specified, by Bonferroni's post hoc test. For all analyses, the significance was $p < 0.05$, indicating a noteworthy distinction between groups. The groups were assessed and depicted for proliferation analysis via median and 95% Confidence Intervals (C.I.). Graphs were plotted in OriginPro 9 (OriginLab Corp, USA).

SUPPLEMENTAL MATERIAL

See the supplementary material for the additional immunofluorescence images of 3D bioprinted hNPCs cultured in NEM and NMM are presented, showing cells expressing NESTIN, GFAP, and TUBB3 (Fig. 1). Quantitative PCR (qPCR) analysis shows the expression of FOXG1 and MAP2 by bioprinted hNPCs over time (Fig. 2). Cell migration within the constructs is illustrated in Fig. 3 and captured in Videos 1 and 2.

ACKNOWLEDGMENTS

We thank Professor Lygia da Veiga Pereira (LaNCE—Embryonic Stem Cell National Laboratory, USP, São Paulo, Brazil)

for the hiPSCs. We thank Professor Cristina Pacheco Soares (UNIVAP, São José dos Campos, Brazil) for assistance with the SEM analysis. We thank Professor Fabiana Perrechil Bonsanto (Laboratory of Biotechnology and Natural Products, BioNat, UNIFESP, Diadema, Brazil) for providing the rheometer for the rheological analysis. We thank Elizabeth N. Kanashiro and Carolina Z. Romera (EPM-UNIFESP, São Paulo, Brazil) for their assistance with the confocal microscopy image captures.

This work was supported by the São Paulo Research Foundation (FAPESP), Grants 2018/12605-8; 2019/08975-7; the National Council for Scientific and Technological Development (CNPq), Grants 465656/2014-5, 406258/2022-8, and 311026/2022-2; and Coordenação de Aperfeiçoamento de Pessoal de Nível Superior (CAPES), finance code 001.

AUTHOR DECLARATIONS

Conflict of Interest

The authors have no conflicts to disclose.

Ethics Approval

Ethics approval is not required.

Author Contributions

Lucas Simões Machado and Paula Scanavez Ferreira contributed equally to this work.

Lucas Simões Machado: Conceptualization (equal); Formal analysis (equal); Investigation (equal); Writing – original draft (lead); Writing – review & editing (equal). **Paula Scanavez Ferreira:** Formal analysis (equal); Investigation (equal); Writing – original draft (lead); Writing – review & editing (equal). **Marina Rodrigues Pires:** Formal analysis (equal); Investigation (equal); Writing – original draft (equal); Writing – review & editing (equal). **Larissa Valdemarin Bim:** Formal analysis (equal); Investigation (equal); Writing – original draft (equal); Writing – review & editing (equal). **Natália Heloísa de Oliveira:** Formal analysis (equal); Investigation (equal); Writing – original draft (equal); Writing – review & editing (supporting). **Geisa Rodrigues Salles:** Formal analysis (equal); Investigation (equal); Writing – review & editing (supporting). **Natalia Dall'Agnol Ferreira:** Formal analysis (supporting); Investigation (supporting). **Elisa Marozzi Cruz:** Formal analysis (equal); Investigation (equal); Writing – original draft (supporting); Writing – review & editing (supporting). **Marimelia Aparecida Porcionatto:** Conceptualization (lead); Data curation (lead); Formal analysis (equal); Funding acquisition (lead); Methodology (supporting); Project administration (lead); Supervision (lead); Writing – original draft (supporting); Writing – review & editing (equal).

DATA AVAILABILITY

The data that support the findings of this study are available from the corresponding author upon reasonable request.

REFERENCES

Alave Reyes-Furrer, A., De Andrade, S., Bachmann, D., Jeker, H., Steinmann, M., Accart, N., Dunbar, A., Rausch, M., Bono, E., Rimann, M., and Keller, H., "Matrigel 3D bioprinting of contractile human skeletal muscle models recapitulating exercise and pharmacological responses," Commun. Biol. **4**, 1183 (2021).

Andreotti, J. P., Silva, W. N., Costa, A. C., Picoli, C. C., Bitencourt, F. C. O., Coimbra-Campos, L. M. C., Resende, R. R., Magno, L. A. V., Romano-Silva, M. A., Mintz, A., and Birbrair, A., "Neural stem cell niche heterogeneity," Semin. Cell Dev. Biol. **95**, 42–53 (2019).

Andrews, M. G. and Kriegstein, A. R., "Challenges of organoid research," Annu. Rev. Neurosci. **45**, 23–39 (2022).

Andrews, M. G., Mukhtar, T., Eze, U. C., Simoneau, C. R., Ross, J., Parikshak, N., Wang, S., Zhou, L., Koontz, M., Velmeshev, D., Siebert, C. V., Gemenes, K. M., Tabata, T., Perez, Y., Wang, L., Mostajo-Radji, M. A., de Majo, M., Donohue, K. C., Shin, D., Salma, J., Pollen, A. A., Nowakowski, T. J., Ullian, E., Renuka Kumar, G., Winkler, E. A., Crouch, E. E., Ott, M., and Kriegstein, A. R., "Tropism of SARS-CoV-2 for human cortical astrocytes," Proc. Natl. Acad. Sci. U. S. A. **119**, e2122236119 (2022).

Andrews, M. G., Subramanian, L., and Kriegstein, A. R., "mTOR signaling regulates the morphology and migration of outer radial glia in developing human cortex," elife **9**, e58737 (2020).

Banerjee, A., Arha, M., Choudhary, S., Ashton, R. S., Bhatia, S. R., Schaffer, D. V., and Kane, R. S., "The influence of hydrogel modulus on the proliferation and differentiation of encapsulated neural stem cells," Biomaterials **30**, 4695–4699 (2009).

Bao, M., Xie, J., and Huck, W. T. S., "Recent advances in engineering the stem cell microniche in 3D," Adv. Sci. **5**, 1800448 (2018).

Bektas, C. K., Luo, J., Conley, B., Le, K. N., and Lee, K. B., "3D bioprinting approaches for enhancing stem cell-based neural tissue regeneration," Acta Biomater. **193**, 20–48 (2025).

Benincasa, J. C., Madias, M. I., Kandell, R. M., Delgado-Garcia, L. M., Engler, A. J., Kwon, E. J., and Porcionatto, M. A., "Mechanobiological modulation of in vitro astrocyte reactivity using variable gel stiffness," ACS Biomater. Sci. Eng. **10**, 4279–4296 (2024).

Bercea, M., "Rheology as a tool for fine-tuning the properties of printable bioinspired gels," Molecules **28**, 2766 (2023).

Bilkic, I., Sotelo, D., Anujarerat, S., Ortiz, N. R., Alonzo, M., Khoury, R. E., Loyola, C. C., and Joddar, B., "Development of an extrusion-based 3D-printing strategy for clustering of human neural progenitor cells," Heliyon **8**, e12250 (2022).

Bose, S., Clevers, H., and Shen, X., "Promises and challenges of organoid-guided precision medicine," Med **2**, 1011–1026 (2021).

Chambers, S. M., Fasano, C. A., Papapetrou, E. P., Tomishima, M., Sadelain, M., and Studer, L., "Highly efficient neural conversion of human ES and iPS cells by dual inhibition of SMAD signaling," Nat Biotechnol **27**, 275–280 (2009).

Chen, X. B., Fazel Anvari-Yazdi, A., Duan, X., Zimmerling, A., Gharraei, R., Sharma, N. K., Sweilem, S., and Ning, L., "Biomaterials/bioinks and extrusion bioprinting," Bioact. Mater. **28**, 511–536 (2023).

Chu, H., Zhang, K., Rao, Z., Song, P., Lin, Z., Zhou, J., Yang, L., Quan, D., and Bai, Y., "Harnessing decellularised extracellular matrix microgels into modular bioinks for extrusion-based bioprinting with good printability and high post-printing cell viability," Biomater. Transl. **4**, 115–127 (2023).

Cooke, M. E. and Rosenzweig, D. H., "The rheology of direct and suspended extrusion bioprinting," APL Bioeng. **5**, 011502 (2021).

Cruz, E. M., Machado, L. S., Zamproni, L. N., Bim, L. V., Ferreira, P. S., Pinto, L. A., Pessan, L. A., Backes, E. H., and Porcionatto, M. A., "A gelatin methacrylate-based hydrogel as a potential bioink for 3D bioprinting and neuronal differentiation," Pharmaceutics **15**, 627 (2023).

Cui, L., Yao, Y., and Yim, E. K. F., "The effects of surface topography modification on hydrogel properties," APL Bioeng. **5**, 031509 (2021).

de Groot, S. C., Sliedregt, K., van Benthem, P. P. G., Rivolta, M. N., and Huisman, M. A., "Building an artificial stem cell niche: Prerequisites for future 3D-formation of inner ear structures-toward 3D inner ear biotechnology," Anat. Rec. **303**, 408–426 (2020).

de Jongh, D., Massey, E. K., Bunnik, E. M., and Vanguard consortium, "Organoids: A systematic review of ethical issues," Stem Cell Res. Ther. **13**, 337 (2022).

de la Vega, L., Lee, C., Sharma, R., Amereh, M., and Willerth, S. M., "3D bioprinting models of neural tissues: The current state of the field and future directions," Brain Res. Bull. **150**, 240–249 (2019).

de Melo, B. A. G., Cruz, E. M., Ribeiro, T. N., Mundim, M. V., and Porcionatto, M. A., "3D bioprinting of murine cortical astrocytes for engineering neural-like tissue," J. Vis. Exp. **173**, e62691 (2021).
Douet, V., Kerever, A., Arikawa-Hirasawa, E., and Mercier, F., "Fractone-heparan sulphates mediate FGF-2 stimulation of cell proliferation in the adult subventricular zone," Cell Proliferation **46**, 137–145 (2013).
Engler, A. J., Sen, S., Sweeney, H. L., and Discher, D. E., "Matrix elasticity directs stem cell lineage specification," Cell **126**, 677–689 (2006).
Fang, W., Yang, M., Wang, L., Li, W., Liu, M., Jin, Y., Wang, Y., Yang, R., Wang, Y., Zhang, K., and Fu, Q., "Hydrogels for 3D bioprinting in tissue engineering and regenerative medicine: Current progress and challenges," Int. J. Bioprint. **9**, 759 (2023).
Ferreira, D. N. A., Ferreira, P. S., Pacheco-Soares, C., Porcionatto, M. A., and Salles, G. R., "3D-bioprinted model of adult neural stem cell microenvironment in Alzheimer's disease," Int. J. Bioprint. **10**, 3751 (2024).
Fu, Z., Hai, N., Zhong, Y., and Sun, W., "Printing GelMA bioinks: A strategy for building in vitro model to study nanoparticle-based minocycline release and cellular protection under oxidative stress," Biofabrication **16**, 025040 (2024).
Fukuda, S., Kato, F., Tozuka, Y., Yamaguchi, M., Miyamoto, Y., and Hisatsune, T., "Two distinct subpopulations of nestin-positive cells in adult mouse dentate gyrus," J. Neurosci. **23**, 9357–9366 (2003).
Gao, T., Gillispie, G. J., Copus, J. S., Pr, A. K., Seol, Y. J., Atala, A., Yoo, J. J., and Lee, S. J., "Optimization of gelatin-alginate composite bioink printability using rheological parameters: A systematic approach," Biofabrication **10**, 034106 (2018).
Giachino, C., Basak, O., Lugert, S., Knuckles, P., Obernier, K., Fiorelli, R., Frank, S., Raineteau, O., Alvarez-Buylla, A., and Taylor, V., "Molecular diversity subdivides the adult forebrain neural stem cell population," Stem Cells **32**, 70–84 (2014).
Gradisnik, L., Bosnjak, R., Maver, T., and Velnar, T., "Advanced bio-based polymers for astrocyte cell models," Materials **14**, 3664 (2021).
Herrada-Manchon, H., Fernandez, M. A., and Aguilar, E., "Essential guide to hydrogel rheology in extrusion 3D printing: How to measure it and why it matters?," Gels **9**, 517 (2023).
Hettige, N. C., Fleming, P., Semenak, A., Zhang, X., Peng, H., Hagel, M. D., Theroux, J. F., Zhang, Y., Ni, A., Jefri, M., Antonyan, L., Alsuwaidi, S., Schuppert, A., Stumpf, P. S., and Ernst, C., "FOXG1 targets BMP repressors and cell cycle inhibitors in human neural progenitor cells," Hum. Mol. Genet. **32**, 2511–2522 (2023).
Hettige, N. C., Peng, H., Wu, H., Zhang, X., Yerko, V., Zhang, Y., Jefri, M., Soubannier, V., Maussion, G., Alsuwaidi, S., Ni, A., Rocha, C., Krishnan, J., McCarty, V., Antonyan, L., Schuppert, A., Turecki, G., Fon, E. A., Durcan, T. M., and Ernst, C., "FOXG1 dose tunes cell proliferation dynamics in human forebrain progenitor cells," Stem Cell Rep. **17**, 475–488 (2022).
Hofer, M. and Lutolf, M. P., "Engineering organoids," Nat. Rev. Mater. **6**, 402–420 (2021).
Huang, Y., Huang, Z., Tang, Z., Chen, Y., Huang, M., Liu, H., Huang, W., Ye, Q., and Jia, B., "Research progress, challenges, and breakthroughs of organoids as disease models," Front. Cell Dev. Biol. **9**, 740574 (2021).
Ioannidis, K., Angelopoulos, I., Gakis, G., Karantzelis, N., Spyroulias, G. A., Lygerou, Z., and Taraviras, S., "3D reconstitution of the neural stem cell niche: Connecting the dots," Front. Bioeng. Biotechnol. **9**, 705470 (2021).
Jahani Kadousaraei, M., Yamada, S., Aydin, M. S., Rashad, A., Cabeza, N. M., Mohamed-Ahmed, S., Gjerde, C. G., Malkoch, M., and Mustafa, K., "Bioprinting of mesenchymal stem cells in low concentration gelatin methacryloyl/alginate blends without ionic crosslinking of alginate," Sci. Rep. **15**, 6609 (2025).
Jensen, K. B. and Little, M. H., "Organoids are not organs: Sources of variation and misinformation in organoid biology," Stem Cell Rep. **18**, 1255–1270 (2023).
Jeong, G. S., Chang, J. Y., Park, J. S., Lee, S. A., Park, D., Woo, J., An, H., Lee, C. J., and Lee, S. H., "Networked neural spheroid by neuro-bundle mimicking nervous system created by topology effect," Mol. Brain **8**, 17 (2015).
Jinnou, H., Sawada, M., Kawase, K., Kaneko, N., Herranz-Perez, V., Miyamoto, T., Kawaue, T., Miyata, T., Tabata, Y., Akaike, T., Garcia-Verdugo, J. M., Ajioka, I., Saitoh, S., and Sawamoto, K., "Radial glial fibers promote neuronal migration and functional recovery after neonatal brain injury," Cell Stem Cell **22**, 128–137.e9 (2018).
Joung, D., Truong, V., Neitzke, C. C., Guo, S. Z., Walsh, P. J., Monat, J. R., Meng, F., Park, S. H., Dutton, J. R., Parr, A. M., and McAlpine, M. C., "3D printed stem-cell derived neural progenitors generate spinal cord scaffolds," Adv. Funct. Mater. **28**, 1801850 (2018).
Kacarevic, Z. P., Rider, P. M., Alkildani, S., Retnasingh, S., Smeets, R., Jung, O., Ivanisevic, Z., and Barbeck, M., "An introduction to 3D bioprinting: Possibilities, challenges and future aspects," Materials **11**, 2199 (2018).
Kadoshima, T., Sakaguchi, H., Nakano, T., Soen, M., Ando, S., Eiraku, M., and Sasai, Y., "Self-organization of axial polarity, inside-out layer pattern, and species-specific progenitor dynamics in human ES cell-derived neocortex," Proc. Natl. Acad. Sci. U. S. A. **110**, 20284–20289 (2013).
Khazaei, M., Ahuja, C. S., Nakashima, H., Nagoshi, N., Li, L., Wang, J., Chio, J., Badner, A., Seligman, D., Ichise, A., Shibata, S., and Fehlings, M. G., "GDNF rescues the fate of neural progenitor grafts by attenuating Notch signals in the injured spinal cord in rodents," Sci. Transl. Med. **12**, eaau3538 (2020).
Khetan, S., Guvendiren, M., Legant, W. R., Cohen, D. M., Chen, C. S., and Burdick, J. A., "Degradation-mediated cellular traction directs stem cell fate in covalently crosslinked three-dimensional hydrogels," Nat. Mater. **12**, 458–465 (2013).
Kim, J., Koo, B. K., and Knoblich, J. A., "Human organoids: Model systems for human biology and medicine," Nat. Rev. Mol. Cell Biol. **21**, 571–584 (2020).
Kitana, W., Levario-Diaz, V., Cavalcanti-Adam, E. A., and Ionov, L., "Biofabrication of composite bioink-nanofiber constructs: Effect of rheological properties of bioinks on 3D (Bio)Printing and cells interaction with aligned touch spun nanofibers," Adv. Healthcare Mater. **13**, e2303343 (2024).
Kothapalli, C., Mahajan, G., and Farrell, K., "Substrate stiffness induced mechanotransduction regulates temporal evolution of human fetal neural progenitor cell phenotype, differentiation, and biomechanics," Biomater. Sci. **8**, 5452–5464 (2020).
Kuhn, H. G., Winkler, J., Kempermann, G., Thal, L. J., and Gage, F. H., "Epidermal growth factor and fibroblast growth factor-2 have different effects on neural progenitors in the adult rat brain," J. Neurosci. **17**, 5820–5829 (1997).
Lamus, F., Martin, C., Carnicero, E., Moro, J. A., Fernandez, J. M. F., Mano, A., Gato, A., and Alonso, M. I., "FGF2/EGF contributes to brain neuroepithelial precursor proliferation and neurogenesis in rat embryos: The involvement of embryonic cerebrospinal fluid," Dev. Dyn. **249**, 141–153 (2020).
Lee, J. H. and Sun, W., "Neural organoids, a versatile model for neuroscience," Mol. Cells **45**, 53–64 (2022).
Li, H., Chen, S., Dissanayaka, W. L., and Wang, M., "Gelatin methacryloyl/sodium alginate/cellulose nanocrystal inks and 3D printing for dental tissue engineering applications," ACS Omega **9**, 48361–48373 (2024).
Li, H., Gan, X., Pan, L., Zhang, Y., Hu, X., and Wang, Z., "EGF/bFGF promotes survival, migration and differentiation into neurons of GFP-labeled rhesus monkey neural stem cells xenografted into the rat brain," Biochem. Biophys. Res. Commun. **620**, 76–82 (2022).
Liang, Y., Qiao, L., Qiao, B., and Guo, B., "Conductive hydrogels for tissue repair," Chem. Sci. **14**, 3091–3116 (2023).
Liour, S. S., Kraemer, S. A., Dinkins, M. B., Su, C. Y., Yanagisawa, M., and Yu, R. K., "Further characterization of embryonic stem cell-derived radial glial cells," Glia **53**, 43–56 (2006).
Lo, C. M., Wang, H. B., Dembo, M., and Wang, Y. L., "Cell movement is guided by the rigidity of the substrate," Biophys. J. **79**, 144–152 (2000).
Lu, D., Chen, C. S., Lai, C. S., Soni, S., Lam, T., Le, C., Chen, E. Y., Nguyen, T., and Chin, W. C., "Microgrooved surface modulates neuron differentiation in human embryonic stem cells," Methods Mol. Biol. **1307**, 281–287 (2016).
Lu, P., Ruan, D., Huang, M., Tian, M., Zhu, K., Gan, Z., and Xiao, Z., "Harnessing the potential of hydrogels for advanced therapeutic applications: Current achievements and future directions," Signal Transduct. Target. Ther. **9**, 166 (2024).
Madl, C. M., LeSavage, B. L., Dewi, R. E., Dinh, C. B., Stowers, R. S., Khariton, M., Lampe, K. J., Nguyen, D., Chaudhuri, O., Enejder, A., and Heilshorn, S. C., "Maintenance of neural progenitor cell stemness in 3D hydrogels requires matrix remodelling," Nat. Mater. **16**, 1233–1242 (2017).

Nadarajah, B., Brunstrom, J. E., Grutzendler, J., Wong, R. O., and Pearlman, A. L., "Two modes of radial migration in early development of the cerebral cortex," Nat. Neurosci. **4**, 143–150 (2001).
Naghieh, S. and Chen, X., "Printability—A key issue in extrusion-based bioprinting," J. Pharm. Anal. **11**, 564–579 (2021).
Orr, A., Kalantarnia, F., Nazir, S., Bolandi, B., Alderson, D., O'Grady, K., Hoorfar, M., Julian, L. M., and Willerth, S. M., "Recent advances in 3D bioprinted neural models: A systematic review on the applications to drug discovery," Adv. Drug Deliv. Rev. **218**, 115524 (2025).
Paredes, M. F., James, D., Gil-Perotin, S., Kim, H., Cotter, J. A., Ng, C., Sandoval, K., Rowitch, D. H., Xu, D., McQuillen, P. S., Garcia-Verdugo, J. M., Huang, E. J., and Alvarez-Buylla, A., "Extensive migration of young neurons into the infant human frontal lobe," Science **354**, aaf7073 (2016).
Regalado-Santiago, C., Juarez-Aguilar, E., Olivares-Hernandez, J. D., and Tamariz, E., "Mimicking neural stem cell niche by biocompatible substrates," Stem Cells Int. **2016**, 1513285.
Rodriguez-Rego, J. M., Mendoza-Cerezo, L., Macias-Garcia, A., Mendoza-Cerezo, L., Carrasco-Amador, J. P., and Marcos-Romero, A. C., "Methodology for characterizing the printability of hydrogels," Int. J. Bioprint. **9**, 667 (2023).
Saha, K., Keung, A. J., Irwin, E. F., Li, Y., Little, L., Schaffer, D. V., and Healy, K. E., "Substrate modulus directs neural stem cell behavior," Biophys. J. **95**, 4426–4438 (2008).
Salaris, F. and Rosa, A., "Construction of 3D in vitro models by bioprinting human pluripotent stem cells: Challenges and opportunities," Brain Res. **1723**, 146393 (2019).
Schaffner, I., Wittmann, M. T., Vogel, T., and Lie, D. C., "Differential vulnerability of adult neurogenic niches to dosage of the neurodevelopmental-disorder linked gene Foxg1," Mol. Psychiatry **28**, 497–514 (2023).
Sharma, R., Smits, I. P. M., De La Vega, L., Lee, C., and Willerth, S. M., "3D bioprinting pluripotent stem cell derived neural tissues using a novel fibrin bioink containing drug releasing microspheres," Front. Bioeng. Biotechnol. **8**, 57 (2020).
Shin, Y., Yang, K., Han, S., Park, H. J., Seok Heo, Y., Cho, S. W., and Chung, S., "Reconstituting vascular microenvironment of neural stem cell niche in three-dimensional extracellular matrix," Adv. Healthcare Mater. **3**, 1457–1464 (2014).
Soltan, N., Ning, L., Mohabatpour, F., Papagerakis, P., and Chen, X., "Printability and cell viability in bioprinting alginate dialdehyde-gelatin scaffolds," ACS Biomater. Sci. Eng. **5**, 2976–2987 (2019).
Soman, S. S. and Vijayavenkataraman, S., "Applications of 3D bioprinted-induced pluripotent stem cells in healthcare," Int. J. Bioprint. **6**, 280 (2020).
Sthanam, L. K., Saxena, N., Mistari, V. K., Roy, T., Jadhav, S. R., and Sen, S., "Initial priming on soft substrates enhances subsequent topography-induced neuronal differentiation in ESCs but not in MSCs," ACS Biomater. Sci. Eng. **5**, 180–192 (2019).
Stojkov, G., Niyazov, Z., Picchioni, F., and Bose, R. K., "Relationship between structure and rheology of hydrogels for various applications," Gels **7**, 255 (2021).
Sun, M., Sun, X., Wang, Z., Guo, S., Yu, G., and Yang, H., "Synthesis and properties of gelatin methacryloyl (GelMA) hydrogels and their recent applications in load-bearing tissue," Polymers **10**, 1290 (2018).
Supeno, N. E., Pati, S., Hadi, R. A., Ghani, A. R., Mustafa, Z., Abdullah, J. M., Idris, F. M., Han, X., and Jaafar, H., "IGF-1 acts as controlling switch for long-term proliferation and maintenance of EGF/FGF-responsive striatal neural stem cells," Int. J. Med. Sci. **10**, 522–531 (2013).
Sutterlin, P., Williams, E. J., Chambers, D., Saraf, K., von Schack, D., Reisenberg, M., Doherty, P., and Williams, G., "The molecular basis of the cooperation between EGF, FGF and eCB receptors in the regulation of neural stem cell function," Mol. Cell. Neurosci. **52**, 20–30 (2013).
Tarricone, G., Carmagnola, I., and Chiono, V., "Tissue-engineered models of the human brain: State-of-the-art analysis and challenges," J. Funct. Biomater. **13**, 146 (2022).
Theus, A. S., Ning, L., Hwang, B., Gil, C., Chen, S., Wombwell, A., Mehta, R., and Serpooshan, V., "Bioprintability: Physiomechanical and biological requirements of materials for 3D bioprinting processes," Polymers **12**, 2262 (2020).
Tuft, B. W., Zhang, L., Xu, L., Hangartner, A., Leigh, B., Hansen, M. R., and Guymon, C. A., "Material stiffness effects on neurite alignment to photopolymerized micropatterns," Biomacromolecules **15**, 3717–3727 (2014).
Vagaska, B., Gillham, O., and Ferretti, P., "Modelling human CNS injury with human neural stem cells in 2- and 3-dimensional cultures," Sci. Rep. **10**, 6785 (2020).
Vorwald, C. E., Gonzalez-Fernandez, T., Joshee, S., Sikorski, P., and Leach, J. K., "Tunable fibrin-alginate interpenetrating network hydrogels to support cell spreading and network formation," Acta Biomater. **108**, 142–152 (2020).
Wakeman, D. R., Redmond, D. E., Jr., Dodiya, H. B., Sladek, J. R., Jr., Leranth, C., Teng, Y. D., Samulski, R. J., and Snyder, E. Y., "Human neural stem cells survive long term in the midbrain of dopamine-depleted monkeys after GDNF overexpression and project neurites toward an appropriate target," Stem Cells Transl. Med. **3**, 692–701 (2014).
Wang, X., Allen, W. E., Wright, M. A., Sylwestrak, E. L., Samusik, N., Vesuna, S., Evans, K., Liu, C., Ramakrishnan, C., Liu, J., Nolan, G. P., Bava, F. A., and Deisseroth, K., "Three-dimensional intact-tissue sequencing of single-cell transcriptional states," Science **361**, eaat5691 (2018).
Wang, Y., Ma, J., Li, N., Wang, L., Shen, L., Sun, Y., Wang, Y., Zhao, J., Wei, W., Ren, Y., and Liu, J., "Microfluidic engineering of neural stem cell niches for fate determination," Biomicrofluidics **11**, 014106 (2017).
Warren, D., Tomaskovic-Crook, E., Wallace, G. G., and Crook, J. M., "Engineering in vitro human neural tissue analogs by 3D bioprinting and electrostimulation," APL Bioeng. **5**, 020901 (2021).
Willis, C. M., Nicaise, A. M., Krzak, G., Ionescu, R. B., Pappa, V., D'Angelo, A., Agarwal, R., Repolles-de-Dalmau, M., Peruzzotti-Jametti, L., and Pluchino, S., "Soluble factors influencing the neural stem cell niche in brain physiology, inflammation, and aging," Exp. Neurol. **355**, 114124 (2022).
Wu, C. C., Lien, C. C., Hou, W. H., Chiang, P. M., and Tsai, K. J., "Gain of BDNF function in engrafted neural stem cells promotes the therapeutic potential for Alzheimer's disease," Sci. Rep. **6**, 27358 (2016).
Xiaorui, L., Fuyin, Z., Xudong, W., Xuezheng, G., Shudong, Z., Hui, L., Dandan, D., Yubing, L., Lizhen, W., and Yubo, F., "Biomaterial inks for extrusion-based 3D bioprinting: Property, classification, modification, and selection," Int. J. Bioprint. **9**, 649 (2023).
Xu, Y., Zhou, J., Liu, C., Zhang, S., Gao, F., Guo, W., Sun, X., Zhang, C., Li, H., Rao, Z., Qiu, S., Zhu, Q., Liu, X., Guo, X., Shao, Z., Bai, Y., Zhang, X., and Quan, D., "Understanding the role of tissue-specific decellularized spinal cord matrix hydrogel for neural stem/progenitor cell microenvironment reconstruction and spinal cord injury," Biomaterials **268**, 120596 (2021).
Yan, Y., Li, X., Gao, Y., Mathivanan, S., Kong, L., Tao, Y., Dong, Y., Li, X., Bhattacharyya, A., Zhao, X., and Zhang, S. C., "3D bioprinting of human neural tissues with functional connectivity," Cell Stem Cell **31**, 260–274.e7 (2024).
Zhang, R., Quan, H., Wang, Y., and Luo, F., "Neurogenesis in primates versus rodents and the value of non-human primate models," Natl. Sci. Rev. **10**, nwad248 (2023).
Zhao, X. and Bhattacharyya, A., "Human models are needed for studying human neurodevelopmental disorders," Am. J. Hum. Genet. **103**, 829–857 (2018).
Zhu, R., Sun, Z., Li, C., Ramakrishna, S., Chiu, K., and He, L., "Electrical stimulation affects neural stem cell fate and function in vitro," Exp. Neurol. **319**, 112963 (2019).